

## ABSTRACT

Title of Thesis:       FUNCTIONALIZED 3D DNA CRYSTALS THROUGH CORE-SHELL AND LAYER-BY-LAYER ASSEMBLY

Ronald McNeil Jr., Master of Science, 2019

Thesis directed by:   Professor Paul Paukstelis  
                                  Department of Chemistry and Biochemistry  
                                  University of Maryland, College Park

A fundamental goal of DNA nanotechnology has been assembly of DNA crystals for use as molecular scaffolds to organize arrays of guest molecules. We use previously described 3D DNA crystals to demonstrate core-shell and layer-by-layer assembly of DNA crystals capable of accommodating tethered guest molecules within the crystals' pervasive solvent channel network. We describe the first example of epitaxial biomacromolecular core-shell crystallization through assembly of the crystals in two or more discrete layers. The solvent channels also allow post-crystallization guest conjugation with layer-specific addressability. We present microfluidics techniques for core-shell crystal growth which unlock greater potential for finely tunable layer properties and assembling complex multifunctional crystals. We demonstrate assembly of these DNA crystals as nanoscale objects much smaller than previously observed. These techniques present new avenues for using DNA to create multifunctional micro- and nanoscale periodic biomaterials with tunable chemical and physical properties.



FUNCTIONALIZED 3D DNA CRYSTALS THROUGH CORE-SHELL  
AND LAYER-BY-LAYER ASSEMBLY

by

Ronald McNeil Jr.

Thesis submitted to the Faculty of the Graduate School of  
the University of Maryland, College Park in partial  
fulfillment of the requirements for the degree of  
Master of Science  
2019

Advisory Committee:

Professor Paul Paukstelis, Chair  
Professor Jeffery Davis  
Professor David Fushman  
Professor Catherine Fenselau



© Copyright by

Ronald McNeil Jr.

2019



## **Acknowledgments**

Many thanks to the Paukstelis research group. Particularly to Dr. Paul Paulstelis for his continued guidance, advice, and patience. Also, to Diana Zhang for her helpful insights on radiolabeling experimentation, to Kaleb Duelge for his assistance with electron microscopy imaging, and to Emily Luteran for her considerable help maintaining my sanity as I prepared this thesis.

A special thanks to Amy Beaven at the University of Maryland Bioscience Imaging Core and Dr. Sz-Chian Liou at the Advanced Imaging and Microscopy Laboratory at the Maryland Nanocenter for their instruction and for the use of their equipment.

My deepest gratitude to my parents, Ronald Sr. and Martha McNeil, without whose unending support I would not be where I am today.

## Contents

Acknowledgments.....	ii
List of Figures.....	iv
List of Tables.....	v
Introduction.....	1
Chapter I – Core-Shell Crystallization of <i>BET66</i> and Kinetic Studies of Epitaxial Layer Growth.....	6
Chapter II – Post-Crystallization and Orthogonal Labeling of Chemically-Functionalized <i>BET66</i> Crystals.....	15
Chapter III –Microfluidics Approaches for <i>BET66</i> Crystal Growth and Labeling.....	23
Chapter IV – Exploring Growth of <i>BET66</i> Nanocrystals and Visualization of the Crystal Lattice by Electron Microscopy.....	29
Conclusions.....	37
Methods.....	40
<i>Oligonucleotide Synthesis and Purification</i> .....	40
<i>Crystallization</i> .....	40
<i>Core-Shell and Layer-By-Layer Crystal Assembly</i> .....	41
<i>Confocal Fluorescence Microscopy</i> .....	42
<i>Shell Growth Kinetics</i> .....	42
<i>Post-Crystallization Labeling</i> .....	43
<i>Quantitation of In-Crystallo Labeling</i> .....	43
<i>FRET Acceptor Photobleaching</i> .....	44
<i>Microcapillary Crystallization and Labeling</i> .....	44
<i>Transmission Electron Microscopy</i> .....	45
Appendices.....	47
<i>Appendix A – Supplemental Shell Growth Kinetics Data</i> .....	47
<i>Appendix B – Structures of Modified Nucleotides Used for Guest Molecule Coupling</i> .....	48
<i>Appendix C – Multi-Dye Crystals via Pre- and Post-Crystallization Labeling</i> .....	49
<i>Appendix D – TEM Images of <i>BET66</i> Crystals Grown On-Grid</i> .....	50
<i>Appendix E – FIJI (ImageJ) Scripts for Collecting Shell Growth Kinetics Data</i> .....	51
References.....	55

## List of Figures

<b>Figure 1.</b> The lattice structure of <i>BET66</i> crystals.....	3
<b>Figure 2.</b> Covalent guest molecule incorporation into the <i>BET66</i> crystal lattice .....	6
<b>Figure 3.</b> Core-shell assembly.....	8
<b>Figure 4.</b> Defects in core-shell crystallization .....	9
<b>Figure 5.</b> Shell growth kinetics .....	10
<b>Figure 6.</b> Layer-by-layer crystal assembly.....	13
<b>Figure 7.</b> Post-crystallization and simultaneous multi-layer labeling.....	17
<b>Figure 8.</b> Multi-dye labeling pre- and post-crystallization .....	18
<b>Figure 9.</b> Multi-dye post-crystallization labeling and orthogonal labeling.....	20
<b>Figure 10.</b> Acceptor photobleaching of multi-dye <i>BET66</i> crystal .....	21
<b>Figure 11.</b> Microfluidics systems designed for in-line crystal growth .....	23
<b>Figure 12.</b> Crystals grown in microfluidics channels .....	25
<b>Figure 13.</b> In-line core-shell assembly of crystals in a microfluidics channel.....	27
<b>Figure 14.</b> TEM images of <i>BET66</i> crystals grown on TEM grids .....	30
<b>Figure 15.</b> Crystal lattice of <i>BET66</i> shown through TEM .....	32
<b>Figure 16.</b> TEM image of a <i>BET66-Δ5':BET66</i> (1:49) crystal.....	33
<b>Figure 17.</b> TEM image of a <i>BET66</i> nanocrystal .....	34
<b>Figure 18.</b> TEM images of crosslinked <i>BET66</i> crystals.....	35

## List of Tables

<b>Table 1.</b> Growth rate of a <i>BET66:BET66-Fluor</i> (49:1) shell over a <i>BET66</i> core .....	11
<b>Table 2.</b> Shell thickness data for multi-shell crystal growth .....	14
<b>Table 3.</b> Inter-layer FRET efficiency from acceptor photobleaching experiments.....	21
<b>Table 4.</b> Excitation/emission wavelengths used for fluorophore visualization.....	42

## Introduction

The chemical properties of DNA make it an ideal material for programmed self-assembly—even in complex mixtures, complementary oligonucleotides are capable of recognizing each other. DNA hybridization bonding has been employed to create structures of many types.<sup>1</sup> These properties have been used extensively to create nanoscale 2D and 3D DNA objects.<sup>2–8</sup> In addition to its robust molecular recognition properties, DNA is an ideal material for many nanostructural applications because it can be easily synthesized to possess specific desired sequences and chemical modifications and can be conjugated to other molecules through straightforward chemical methods. Nanoscale DNA structures have found applications as templates for positioning organized arrays and assortments of nanoparticles,<sup>9–17</sup> colloids,<sup>18</sup> and proteins,<sup>19–23</sup> as well as in creating thin films and vesicles.<sup>24–28</sup> It has been a long-standing objective within the field of DNA nanotechnology to create three-dimensional DNA crystals, which would facilitate development of periodic molecular scaffolds for positioning and orienting arrays of guest molecules within the crystal lattice.<sup>29</sup> Organization of guest molecules within a DNA lattice is an important milestone toward fulfilling many proposed applications,<sup>30</sup> including the use of DNA lattices as molecular scaffolding to assist in protein crystal structure determination,<sup>29</sup> as biochip devices for molecular-scale storage of information,<sup>31</sup> and as molecular sieves for size-selective molecular sorting<sup>32</sup> and/or catalysis.<sup>33–35</sup>

Core-shell assembly of nanomaterials is an essential method for creating particles and materials with multiple localized functionalities for a variety of applications.<sup>36–41</sup> The primary mechanism for forming core-shell assemblies from small molecules is epitaxial growth, wherein a shell layer propagates from a core crystal.<sup>42,43</sup> Several strategies have

been developed for performing epitaxial growth of protein crystals from various surfaces<sup>44-48</sup> and DNA has previously been used as a connective support for assembly of nanoparticle superlattices.<sup>23</sup>

The *BET66* oligonucleotide, d(GGA CAG CTG GGA G), which self-assembles in the presence of divalent cations ( $Mg^{2+}$  or  $Ca^{2+}$ ), crystallizes to form a porous three-dimensional biomaterial. The high-resolution crystal structures of crystals from *BET66* and related DNA sequences showed that interactions between DNA strands involve both Watson-Crick and noncanonical base pairing motifs (**Figure 1a**).<sup>49,50</sup> Two primary regions of base-base interactions are responsible for the structure of these crystals. The self-complementary duplex region is comprised of six base pairs which are formed by anti-parallel base pairing of two monomer strands under the traditional Watson-Crick model. The interlayer junction region is composed of two sets of three homopurine base pairs ( $G_1 \cdot G_{10}$ ,  $G_2 \cdot G_{11}$ , and  $A_3 \cdot A_{12}$ ). Extensive intra- and interstrand purine-purine stacking interactions provide additional stability to the lattice. The structure of these noncanonical base pairs is predictable and has been used to design other DNA crystals through changing or extending the anti-parallel duplex region.<sup>32,33,50</sup> The noncanonical base pairs of the interlayer junction regions connect each duplex layer to adjacent layers with approximately 2nm spacing between each helix. This spacing creates an internal network of solvent channels throughout the length of the lattice which run parallel (**Figure 1b**) and perpendicular (**Figure 1c**) to the six-fold symmetry axis of the crystal. The space within this solvent channel network is sufficient to accommodate small guest molecules covalently attached to the DNA without disrupting the lattice structure.<sup>50,51</sup> In this work, we demonstrate the ability to visualize these solvent channels using transmission electron

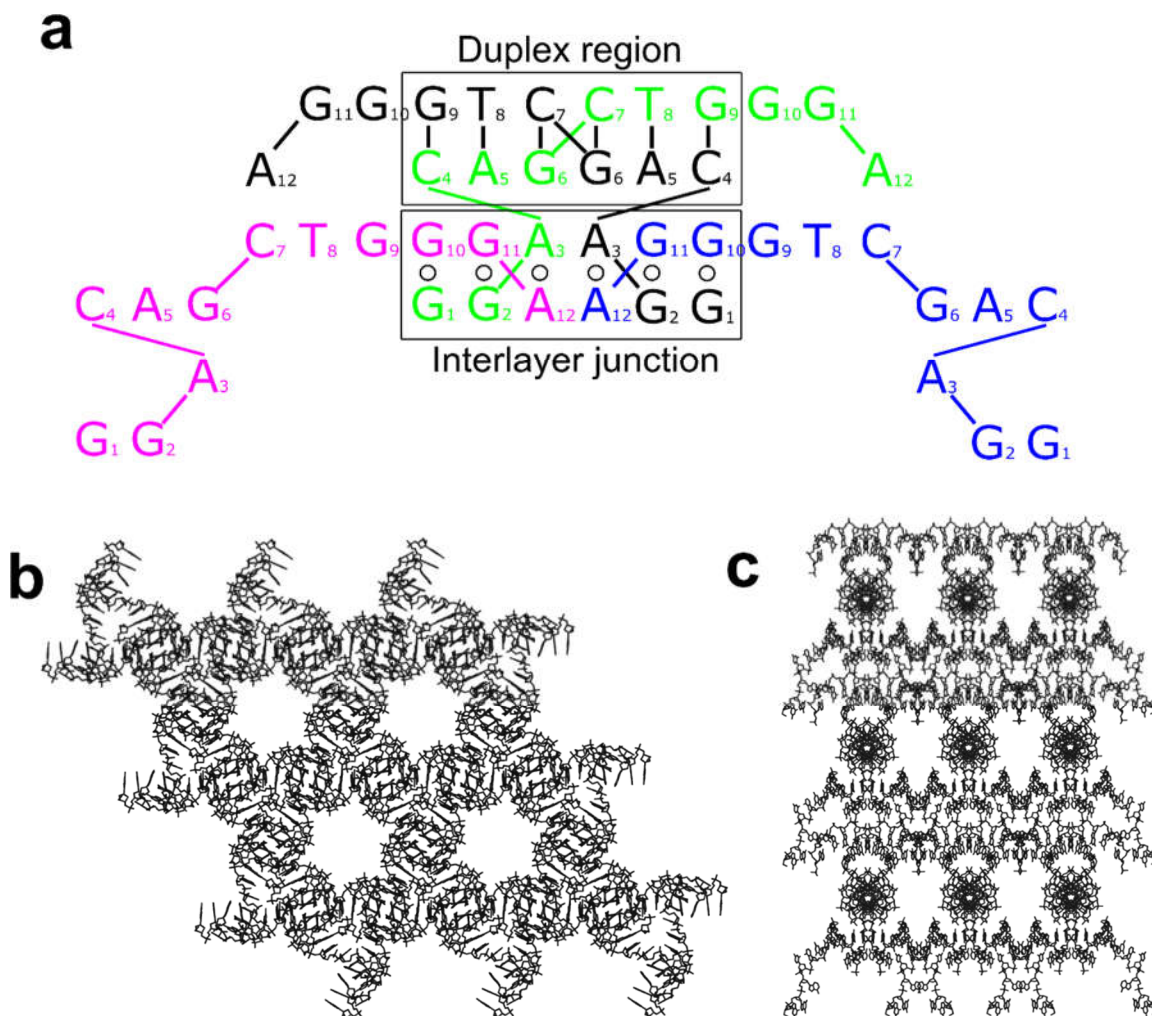


**Figure 1.** The lattice structure of BET66 crystals

(a) Secondary structure of the *BET66* crystal lattice. Four strands are represented in different colors and are related by crystallographic symmetry. Solvent channel networks created by crystal lattice packing run both (b) parallel and (c) perpendicular to the six-fold axis of symmetry.

microscopy methods which are similar to those previously employed for visualization of protein nanocrystals.<sup>52-54</sup> The self-assembly process for *BET66* crystals is dependent upon the presence of sufficient concentrations of a divalent cation ( $Mg^{2+}$  or  $Ca^{2+}$ ). Solution NMR studies showed that *BET66* forms duplex structures and higher-order precursors in the presence of divalent cations, which indicates the crystal self-assembly proceeds through a nonclassical mechanism, rather than classical monomer-by-monomer addition.<sup>50,55</sup>

Here, we expand upon *BET66* crystal self-assembly by describing their ability to undergo core-shell and layer-by-layer assembly and functionalization. Oligonucleotides with identical sequences but varying chemical modifications or covalently attached guest molecules grow epitaxially from a crystal core to produce discrete layers. Confocal microscopy studies of shell layers containing covalently attached fluorophore guests suggest that shell growth is preferential across specific crystal faces and kinetic studies show that shell growth is biphasic with a short initial fast-growth phase followed by a much longer slow-growth phase. The crystal solvent channel network provides sufficient space not only to accommodate the attached guest molecules, but also for guest molecules to be absorbed into the crystal and be covalently attached to specific sites *in crystallo*. This affords two options for attaching guest molecules that we refer to as pre- and post-crystallization guest molecule conjugation. The versatility of these two methods provides new possibilities for creating multi-functionalized periodic biomaterials. In addition, we explore various techniques for producing core-shell and layer-by-layer growth of *BET66* crystals in the laboratory. Of particular interest to us were microfluidics-based approaches, due to their wide variety of application, including protein crystallization, and the high degree of control that they afford.<sup>56-60</sup> We explored a variety of microfluidics-based

approaches for *BET66* crystal growth and have demonstrated proof-of-concept for the technique. *BET66* crystals and core-shell crystals were successfully grown in microfluidic devices. We see this as the first step toward a reproducible high-throughput method for crystals with tunable size and layer properties. Finally, in pursuit of ideal tunability in crystal properties we explored techniques for decreasing the growth size of *BET66* crystals. With the goal of ultimately developing a technique for reproducibly manufacturing *BET66* nanocrystals, we explored alternate buffering conditions for crystallization to facilitate higher numbers of nucleation events and smaller crystals. We employed TEM methods to visualize the resulting particles, accurately measure their size, and verify the crystal lattice structure.

We have demonstrated, for the first time, the assembly of core-shell crystals of a biomacromolecule using epitaxial shell growth from a three-dimensional core crystal.<sup>51</sup> These crystals are composed of a DNA lattice which is able to act as a substrate for homoepitaxial growth of subsequent shell layers. The methods described here provide new avenues for the design of multifunctional micro- and nanoscale biomaterials from periodic 3D DNA lattices potentially useful in a variety of applications.

## Chapter I – Core-Shell Crystallization of *BET66* and Kinetic Studies of Epitaxial Layer Growth

*The contents of this chapter are adapted from McNeil, R. & Paukstelis, P. J. Core-Shell and Layer-by-Layer Assembly of 3D DNA Crystals. Adv. Mater. 29, 1701019 (2017).*

In order to investigate core-shell crystallization using *BET66*, we examined the ability of unlabeled crystal cores to act as macroseeds for epitaxial growth in a model similar to core-shell crystallization of small molecules. To allow visualization of the shell layer, *BET66-Fluor* was included in the shell oligonucleotide solution as a fluorescent indicator. *BET66-Fluor* was not found to interfere with crystal formation and was able to crystallize as a pure sample or as a mixture with unmodified *BET66* (**Figure 2**). This

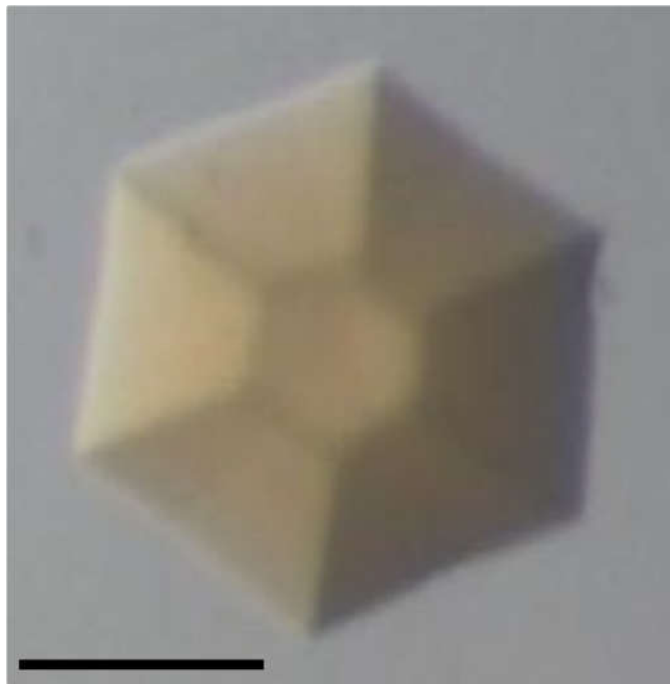


**Figure 2.** Covalent guest molecule incorporation into the *BET66* crystal lattice

An optical microscope image of a 9:1 *BET66*:*BET66-Fluor* crystal. The yellow tint results from the incorporation of fluorescein guest molecules. Scale bar 50  $\mu\text{m}$ .

indicates that the base pairing interactions required to form the crystal lattice structure were not disrupted by the 3'-linked guest molecules. Crystal cores of hexagonal pyramid morphology (**Figure 3a**) were generated using the standard self-assembly method for *BET66*. The cores were transferred to fresh crystallization buffer containing a mixture of *BET66* and *BET66-Fluor* in a 49:1 ratio and incubated. Crystals were washed and then examined by confocal fluorescence microscopy. We observed the accumulation of a discrete fluorescent shell layer over the surface of the entire core crystal (**Figure 3b**). The bases of the hexagonal pyramids—or the (001) crystal face—showed a uniform fluorescent layer which was consistently the thickest region of the shell, ranging from approximately 12 to 16  $\mu\text{m}$  (**Figure 3c**). Typically, the shell layer on each of the six sides of the pyramid showed a uniform thickness which was approximately 50% of the thickness of the shell on the pyramid's base. However, in some cases we observed a crystal which did not show a fluorescent shell layer on either the base or on one side. We attribute this to the orientation of the macroseed during shell growth. Presumably, the face of the crystal with no shell was adhered to the polystyrene crystallization dish surface during assembly of the shell layer (**Figure 4a**). We also observed the appearance of satellite crystals growing from the shell layers in some cases (**Figure 4b**). These crystals appeared most often following multiple shell assemble steps—therefore, multiple crystal handling procedures—suggesting that manipulation of the crystals using nylon loops may introduce defects in the surface which, though they are not independently evident in microscope images, can result in high-angle grain boundaries that may manifest as satellite crystal growth. Roughly 15% of crystals contained one or more satellite crystals, with the size and number of satellite crystals dependent on shell growth time and the amount of crystal handling. Satellite crystals which

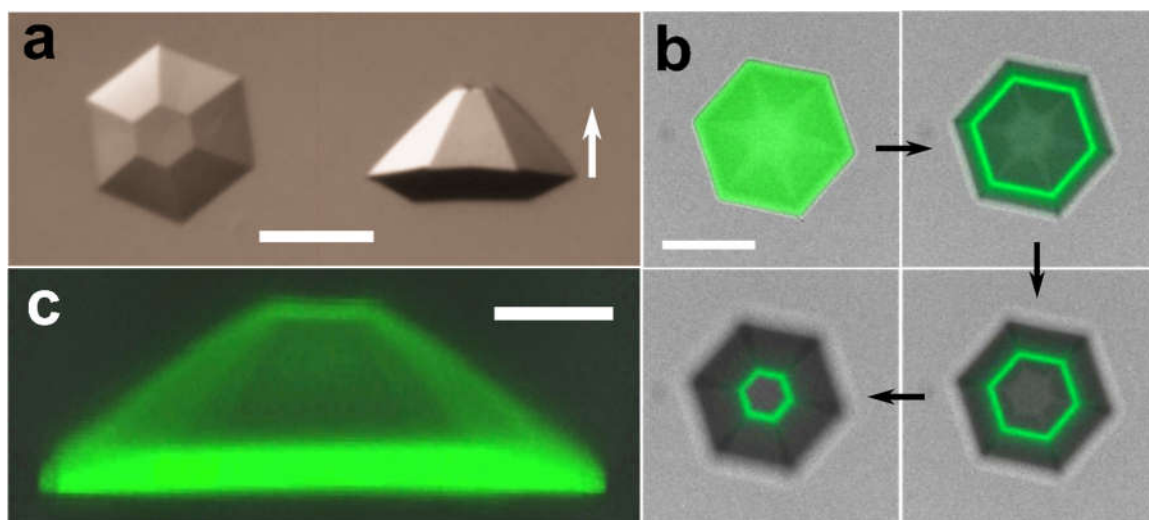


**Figure 3.** Core-shell assembly

(a) Optical microscope images of an unlabeled *BET66* crystal, shown along (left) and orthogonal to (right) the six-fold axis of symmetry. Arrow references the scanning direction along the *z*-axis in subsequent confocal microscope image series. Scale bar 50  $\mu\text{m}$ . (b) Representative images from a confocal *z*-stack series of a core-shell crystal containing an unlabeled *BET66* core and a *BET66*:*BET66-Fluor* (49:1) shell. The scan begins at the crystal base (first panel) and continues in the positive *z* direction through the remaining panels, as indicated by the arrows. Scale bar 50  $\mu\text{m}$ . (c) Side view from a three-dimensional reconstruction of a core-shell crystal with the same composition as the crystal in (b). Scale bar 25  $\mu\text{m}$ .

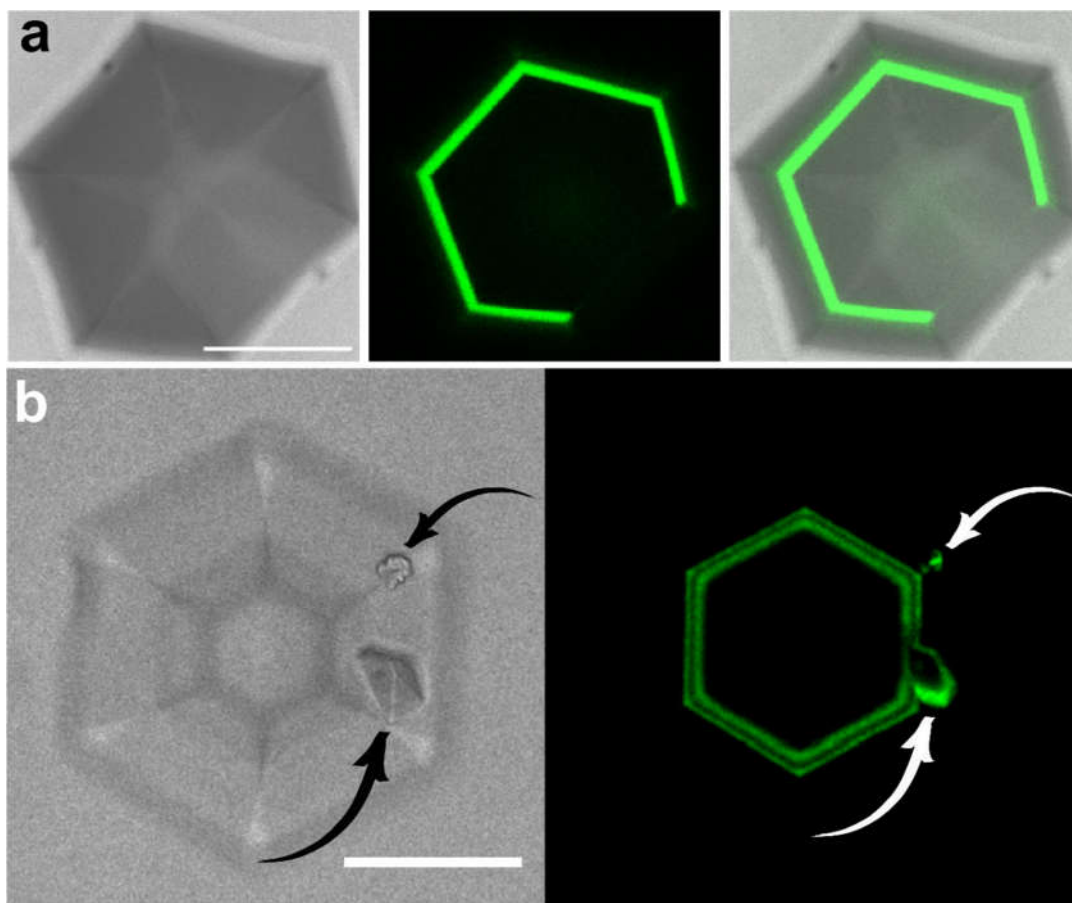


**Figure 4.** Defects in core-shell crystallization

**(a)** *BET66* crystal core with five-sided fluorescent shell layer of *BET66:BET66-Fluor* (49:1) showing one side of the shell is absent. Left to right: bright field, fluorescein emission, and overlaid channels. Scale bar 50  $\mu\text{m}$ . **(b)** An example of satellite crystals (arrows) grown on a striated *BET66* crystal with alternating fluorescent and non-fluorescent layers. Left: bright field. Right: fluorescein emission. Scale bar 50  $\mu\text{m}$ .

form as a result of this process are also capable of growing their own shell layers if subjected to further shell assembly steps, as shown in the fluorescein emission channel of Figure 4b.

In an effort to better understand the dynamics and kinetics of core-shell assembly, growth of crystal shell layers was monitored in real-time using confocal fluorescence microscopy (Figure 5). The shell growth data for both the base and sides of the crystal showed apparent biphasic linear accumulation over the studied time period—growth rate data are presented in Table 1. The first phase was defined by a relatively short period of

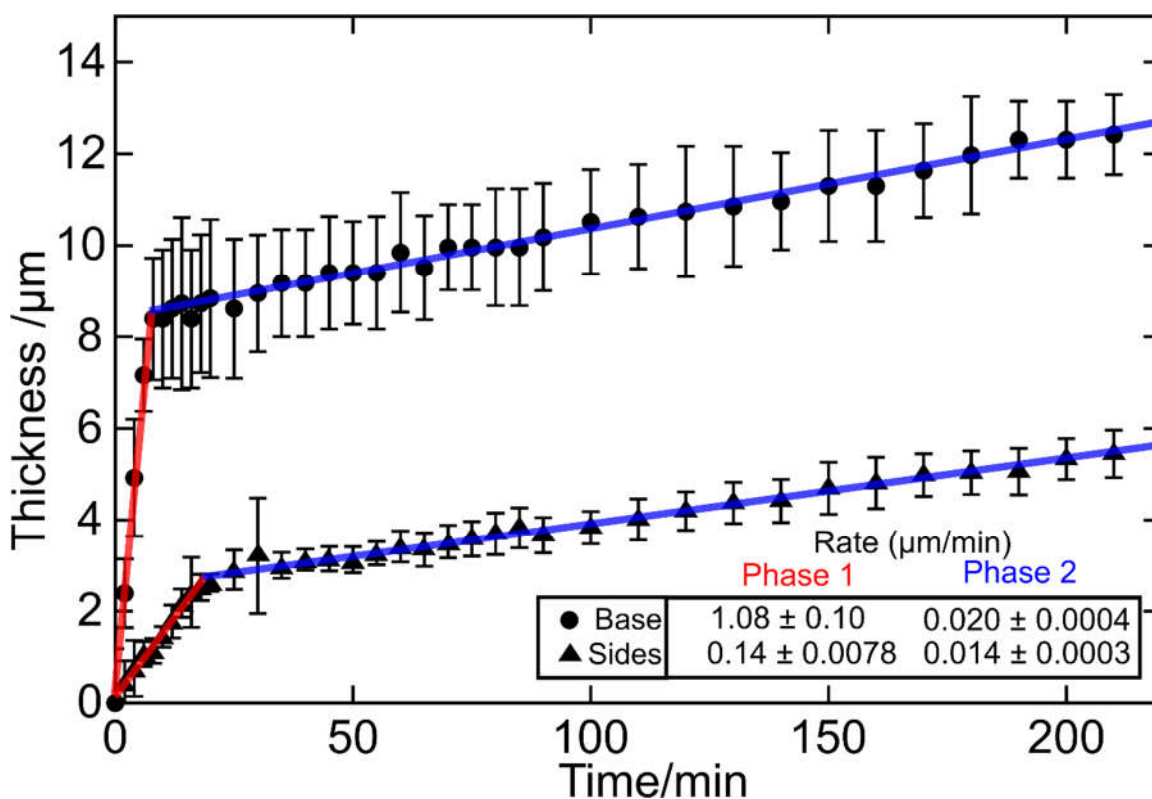


**Figure 5.** Shell growth kinetics

Time-resolved measurements of shell thickness on the base and sides of a single *BET66* crystal during the course of shell self-assembly. Best fit lines are shown for both phases of shell growth, with growth rates shown in the legend. Each data point represents the mean of multiple measurements made using an image analysis script, as described in the methods section. Error bars represent standard deviation.

**Table 1.** Growth rate of a *BET66*:*BET66-Fluor* (49:1) shell over a *BET66* core

	<sup>a</sup> Growth Rate ( $\mu\text{m}/\text{min}$ )	
	Phase 1	Phase 2
Base	1.08 +/- 0.10	0.020 +/- 0.00040
Sides	0.14 +/- 0.0078	0.014 +/- 0.00030

<sup>a</sup> Monitored over 3.5 hr via confocal fluorescence microscopy and calculated as the slope of the best fit lines for the average of multiple measurements.

rapid accumulation—approximately 8 minutes down the six-fold axis (on the base of the pyramid) and approximately eight-fold slower and lasting about 18 minutes on the sides of the crystal. The rates of growth for the base and sides were comparable during the second phase, lasting until the conclusion of data collection at 3.5 hours. There were variations in the measured rates of growth and the duration of each phase for different crystals (**Appendix A**). In all cases biphasic growth was observed and the relative rates between the base and sides were comparable within each phase, respectively.

The biphasic nature of layer growth may be the result of multiple contributing factors, but it is likely linked to the nonclassical crystallization mechanism indicated by previous experiments.<sup>50</sup> A distinguishing feature of these mechanisms is the evolution of precursor species over time.<sup>55</sup> The rapid first phase of growth is consistent with early precursor units of *BET66* being readily incorporated onto the crystal macroseed, following along with the knowledge that *BET66* forms higher-order oligomers when magnesium ions are added to the solution. In this model, the slower second phase is the result of changes in kinetic and thermodynamic properties for incorporation as the precursors evolve into higher molecular weight complexes and changes to the equilibrium of this process as the total concentration of unincorporated *BET66* in solution decreases. The preferential layer

growth along the six-fold axis of symmetry on the crystal base is likely an inherent property of the crystal structure organization. *BET66* and related sequences crystallize as hexagonal unipyramids, which indicates that there is an intrinsic preference for anisotropic growth along the six-fold symmetry axis. This preference is, in part, explained by structural analysis of the crystals, which showed that 5'-G<sub>1</sub>G<sub>2</sub>A<sub>3</sub> residues of the noncanonical base pairing motif of the inter-layer junction are oriented down this axis.<sup>49</sup> When these residues are unpaired, they extend out from the (001) face of the crystal and are available as a cooperative anchoring surface for *BET66* precursors. This model is supported by the demonstration that the 5'-truncated analog, *BET66-Δ5'*, which eliminates these interactions, functions as a crystal habit modifier at low concentrations to specifically restrict growth down the six-fold axis—drastically changing the crystal morphology—or as a “poison” oligomer at higher concentrations to inhibit crystal growth.<sup>61</sup>

To further demonstrate that this core-shell crystallization approach can be employed as a technique for layer-by-layer assembly, we produced striated crystals by exposing a crystal core to three consecutive assembly steps. To visually differentiate between the shell layers, an unlabeled layer was grown between the two *BET66*:*BET66-Fluor* (49:1) layers. **Figure 6a** and **b** show two crystals with this configuration, displaying four distinct layers. The shell growth times for each shell were held constant, and the first two layers were consistently the thickest. The thicknesses of the first (inner), second, and third (outer) shells were 1.80 +/- 0.375 μm, 1.71 +/- 0.247 μm, and 1.32 +/- 0.245 μm, respectively, as determined from the fluorescence profile data (**Figure 6c**). The reasons for the observed decrease in layer thickness have not been fully investigated but are likely related to accumulation of defects on the crystal or other factors associated with increased

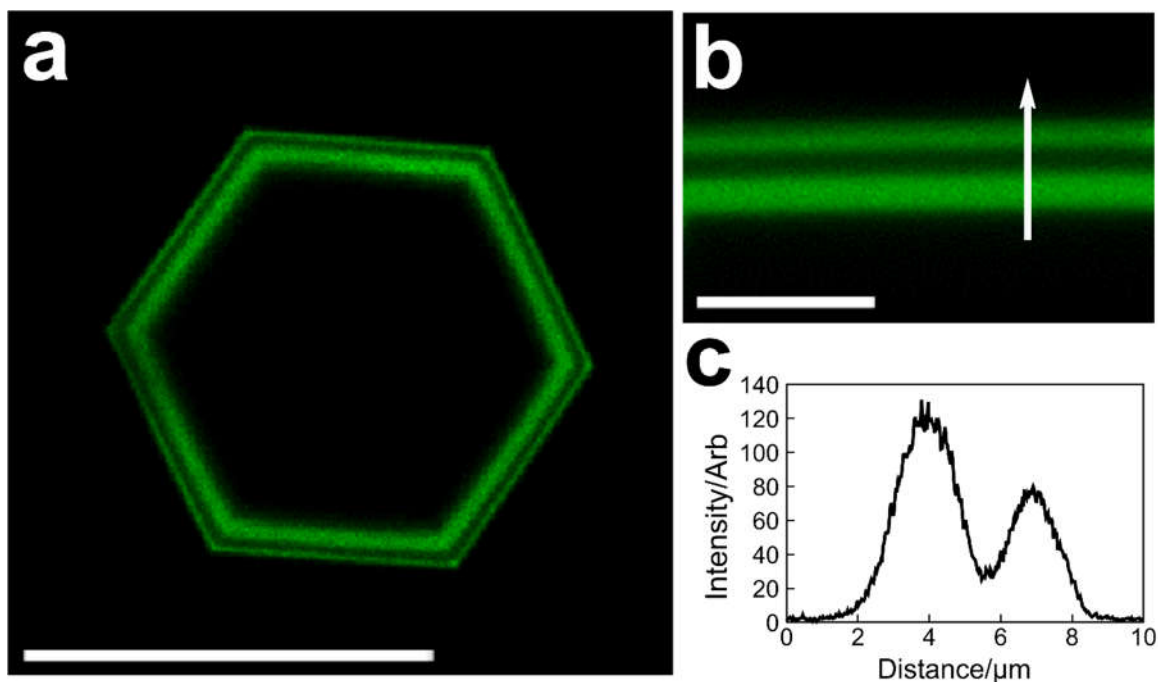


**Figure 6.** Layer-by-layer crystal assembly

(a) Striated crystal generated through layer-by-layer assembly. Scale bar 100  $\mu\text{m}$ . (b) Expanded view of the layer interface, showing each distinct layer—an unlabeled core and three shell layers, two of which are fluorescein-labeled. Scale bar 10  $\mu\text{m}$ . (c) Fluorescence intensity profile in arbitrary units across the arrow shown in (b).

handling during intermediate washing steps.

The thickness of the shell layers was found to be tunable by varying the incubation time, concentration of oligomers, and concentration of buffer constituents. Increased incubation times led to expected increases in overall shell thickness for a given layer (**Table 2**). In addition, a higher concentration of magnesium ions during incubation also resulted in increased shell thickness. This is presumably due to changes in the maturation and incorporation of higher order precursor species in solution. We noted that, for the conditions tested, crystals achieved maximum shell growth for a given layer within a 24-hour incubation period (data not shown). The most likely explanation for this is the

**Table 2.** Shell thickness data for multi-shell crystal growth

Mg <sup>2+</sup>	120 mM						240 mM								
Growth Time	4			16			1			2			4		
<sup>a</sup> Shell Layer	1	2	3	1	2	3	1	2	3	1	2	3	1	2	3
<sup>b</sup> Mean Shell Width	3.84 (1.13)	3.61 (1.03)	1.64 (0.30)	4.92 (1.57)	4.97 (0.82)	3.00 (0.61)	2.30 (0.51)	2.16 (0.54)	1.83 (0.38)	3.28 (1.02)	3.23 (0.81)	2.95 (0.80)	4.08 (0.67)	3.75 (0.73)	3.23 (0.71)

<sup>a</sup> Shells 1 and 3 contain 3'-fluorescein-labeled oligomers as described.

<sup>b</sup> Values represent 16 measurements from at least two crystals. Standard deviations in parentheses.

decreasing concentrations of free DNA and magnesium as the shell grows, eventually falling below a threshold capable of driving further incorporation.

Using *BET66* crystals, we have demonstrated epitaxial core-shell crystallization of a continuous biomacromolecule lattice. There is a consistent preference for growth down the six-fold axis of symmetry during initial crystallization and during shell formation. This suggests that the mechanism of growth is the same or very similar in both cases. The characteristic anisotropic growth of these crystals is a result of the lattice properties and, majorly, the noncanonical base pairs which form an integral part of the crystal structure.

## Chapter II – Post-Crystallization and Orthogonal Labeling of Chemically-Functionalized *BET66* Crystals

*The contents of this chapter are adapted from McNeil, R. & Paukstelis, P. J. Core-Shell and Layer-by-Layer Assembly of 3D DNA Crystals. Adv. Mater. 29, 1701019 (2017).*

A potential limitation of conjugating guest molecules prior to crystallization of *BET66* is their disruption of the interactions necessary for crystal formation due to their size, competition to interact with the DNA, degree of hydrophobicity, or instability during oligonucleotide synthesis. To mitigate these factors and potentially increase the diversity of guest molecules that can be conjugated, we explored techniques for post-crystallization attachment of guest molecules. In order to demonstrate that coupling sites are accessible via the crystal's network of solvent channels, maleimide-functionalized small molecule dyes were covalently attached uniformly throughout the crystal post-crystallization. The C4-thiol-functionalized *BET66-C4-SH* (structures of modified nucleotides shown in **Appendix B**) readily crystallized and, following incubation with fluorescein-maleimide and extensive washing to remove excess dye, the crystals exhibited nearly uniform fluorescence throughout (**Figure 7a**). The apparent decrease in fluorescence intensity toward the center of each hexagonal slice of the z-stack series most likely results from inner-filter effects,<sup>62</sup> contributed to by the relatively high density of fluorophores within the crystal lattice and the sample thickness. Control experiments in which crystals of non-thiolated *BET66* were subjected to identical procedures showed no accumulation of fluorescence, indicating that the washing protocol was sufficient to remove excess dye from the interior of the crystals and no significant dye/oligonucleotide interaction occurred. To determine the efficiency and extent of the dye labeling reaction over time, *BET66-C4-*

*SH* crystals were dye-labeled, washed, dissolved, and finally labeled with  $^{32}\text{P}$ -ATP before being separated by gel electrophoresis to confirm the covalent linkage between the dye-maleimide and the thiolated oligonucleotides of the crystals (**Figure 7b**). Conjugation was shown to be time-dependent and showed quantitative yields—98%—after six hours. This technique for post-crystallization labeling was combined with core-shell crystal growth to provide layer-specific incorporation of dyes. Crystals composed of a *BET66* core and a *BET66-C4-SH* shell showed fluorescence singly throughout the thiol-containing shell layer after incubation with fluorescein-maleimide (**Figure 7c**). The post-crystallization labeling technique was confirmed with another dye—Cy5-maleimide. This dye maleimide was readily coupled to *BET66-C4-SH* despite its higher molecular weight compared to fluorescein. This dye was used to demonstrate simultaneous labeling of multiple layers following completion of crystal growth. Crystals with *BET66-C4-SH* in the core, *BET66* as an unlabeled shell, and *BET66-C4-SH* as a second shell were assembled and incubated with Cy5-maleimide dye as described. Confocal microscopy examination of the crystals showed uniform labeling of the *BET66-C4-SH* layers with Cy5, and no fluorescence within the intermediate *BET66* shell (**Figure 7d and e**).

We believe the capability to combine both pre- and post-assembly incorporation of guest molecules would be useful in generating multifunctional crystals with distinct layers for applications. In light of this, we assembled a core-shell crystal using a core of *BET66:BET66-Fluor* (49:1), followed by growth of a *BET66:BET66-C4-SH* (49:1) shell and subsequent incubation with Cy5-maleimide. Examination by confocal microscopy showed two distinct fluorescent layers, with minimal overlap between the fluorescein-labeled core and the Cy5-labeled shell (**Figure 8a and b**). A 3D reconstruction of the

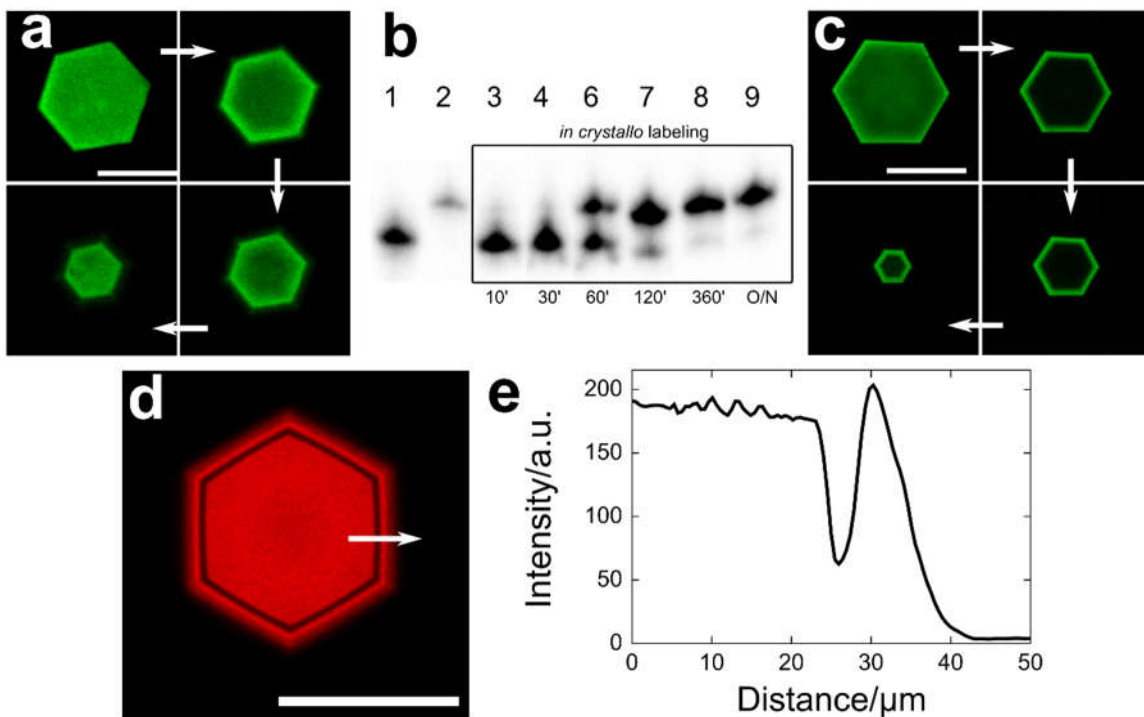


**Figure 7.** Post-crystallization and simultaneous multi-layer labeling

(a) *BET66-C4-SH* crystal labeled with fluorescein-maleimide post-crystallization. Scale bar 100  $\mu\text{m}$ . (b) Gel analysis of labeling. Lane 1, *BET66* control; Lane 2, *BET66-C4-SH* solution labeled with fluorescein; Lanes 3-9, *in crystallo* labeling of *BET66-C4-SH* with fluorescein. Each time point represents two dissolved crystals. (c) Layer-specific post-crystallization labeling of a crystal with *BET66* core and *BET66:BET66-C4-SH* (49:1) shell with fluorescein. Scale bar 100  $\mu\text{m}$ . (d) Simultaneous post-crystallization labeling of multiple layers with Cy5-maleimide. Confocal microscope image of a crystal with a *BET66:BET66-C4-Cy5* (49:1) core, a *BET66* first shell, and a *BET66:BET66-C4-Cy5* (49:1) second shell. Scale bar 100  $\mu\text{m}$ . (e) Fluorescence intensity profile across the crystal layers as indicated by the arrow in (d).

crystals from confocal z-stack image series confirmed that the fluorescein-labeled core was fully encapsulated by the Cy5-labeled shell (**Figure 8c, d, and e**). Combining the techniques for pre- and post-crystallization labeling allowed us to create crystals with a variety of multi-dye combinations using *BET66-Fluor*, *BET66* for blank layers, and *BET66-C4-SH*—labeled with Cy5 after complete crystal/shell assembly (**Appendix C**). In addition, multi-dye crystals can be generated through post-crystallization labeling. The incorporation of various guest molecules within the same crystal while using the same structural material—*BET66-C4-SH*, in this case—demonstrates the versatility and

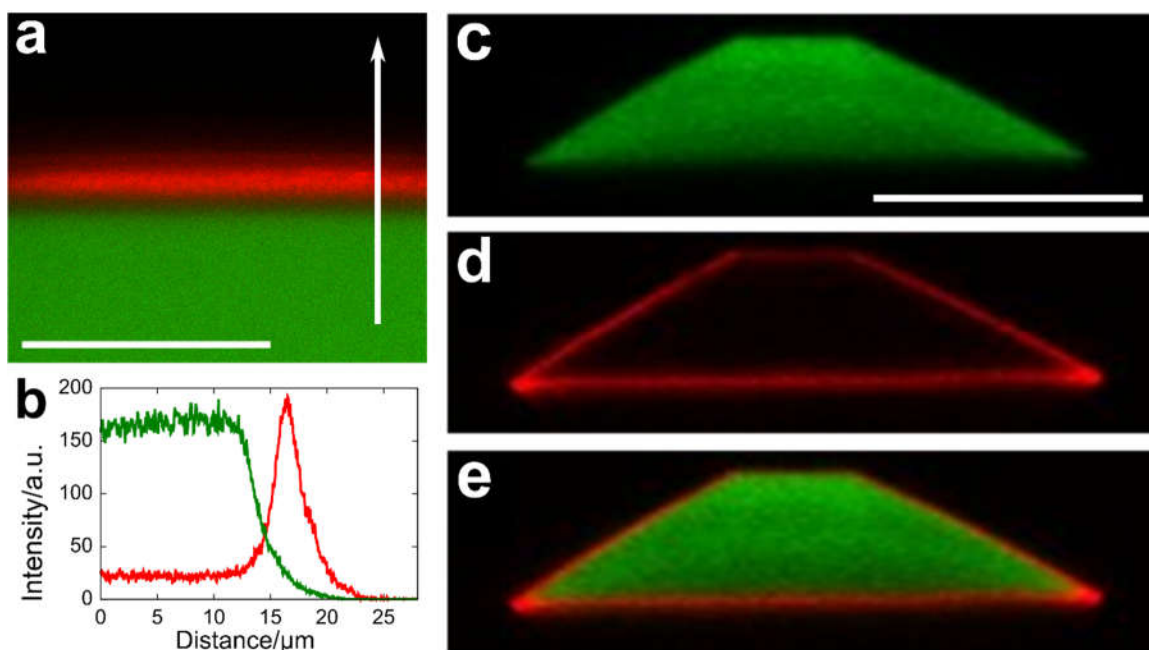


**Figure 8.** Multi-dye labeling pre- and post-crystallization

(a) Layer-specific incorporation of dyes using multiple methods. Confocal microscope image of a crystal with a *BET66:BET66-Fluor* (49:1) core and a *BET66:BET66-C4-Cy5* (49:1) shell—labeled post-crystallization. Fluorescein and Cy5 channels overlaid. Scale bar 20 μm. (b) Fluorescence intensity profile across the crystal layers as indicated by the arrow in (a). (c-e) A vertical cross-section from the 3D reconstruction of the z-stack series of a crystal with the described composition, showing the fluorescein, Cy5, and overlaid channels, respectively. Scale bar 100 μm.

robustness of the technique. This was shown experimentally by sequential incorporation and respective labeling of two *BET66-C4-SH* shells with fluorescein-maleimide and Cy-5 maleimide dyes. Alternating layer growth with dye conjugation steps produced two discrete shell layers of dye-labeled *BET66-C4-SH*, with the inner and outer shells identifiable by unique dye labels—fluorescein-maleimide and Cy5-maleimide, respectively (**Figure 9a**). Multi-dye crystals were also generated through simultaneous orthogonal post-crystallization labeling. This technique takes advantage of the fact that certain chemical reactions can occur simultaneously in the same solution without causing interference with each other. In this experiment, a different functional group was used within each layer of the crystals to direct dye conjugation to the desired layer. In this case, we chose to use the coupling reactions of amine/NHS-ester and thiol/maleimide, as they can occur orthogonally under certain buffer conditions. Crystals with a core of *BET66:BET66-T8-C2N* (9:1) and a shell of *BET66-C4-SH* shell were assembled and incubated with a dye mixture containing amine-reactive Alexa Fluor 532 NHS-ester and thiol-reactive Cy5-maleimide. After thorough washing, the resulting crystals were examined and showed differentially labeled core and shell regions (**Figure 9b**). This demonstrates successful layer-specific addressing of two different guest molecules using orthogonal conjugation reactions for simultaneous incorporation. This simplifies the procedure of labeling multi-layered crystals by reducing the number of individual steps required when multiple guest molecules can be conjugated simultaneously while avoiding interference between the reactions.

We performed FRET experiments to investigate the interaction of guest molecules in adjacent layers. This demonstration is important to certain applications, such as in light-

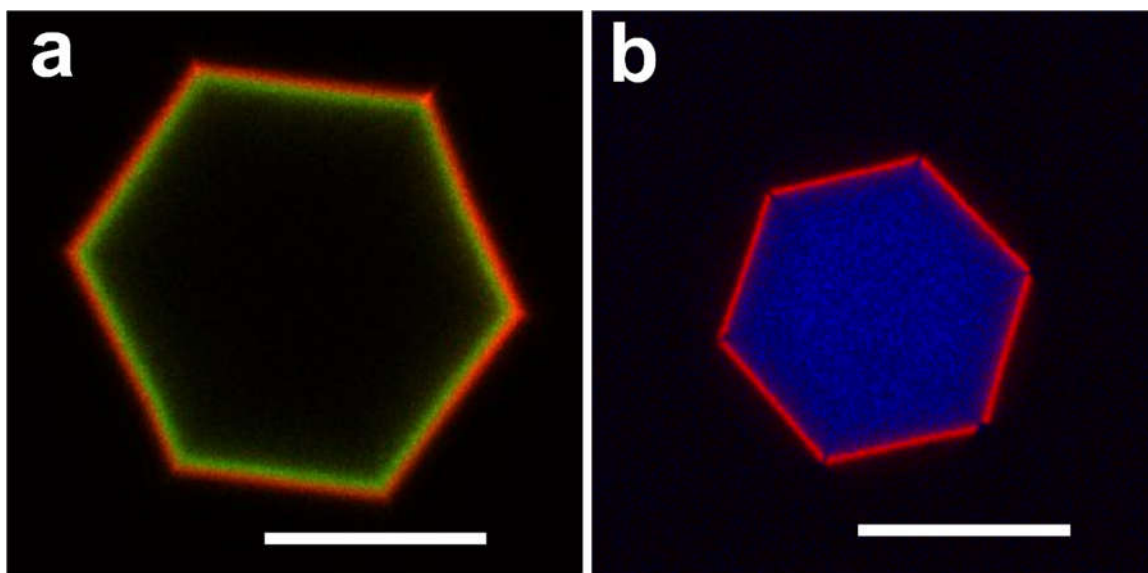


**Figure 9.** Multi-dye post-crystallization labeling and orthogonal labeling

Multi-dye crystals produced by sequential dye conjugation and orthogonal labeling. **(a)** A *BET66-C4-SH* shell was grown and incubated with fluorescein-maleimide, followed by growth and labeling of a second *BET66-C4-SH* shell layer with Cy5-maleimide. Dye conjugation at each step was performed for one hour. **(b)** Simultaneous orthogonal labeling of a core-shell crystal with *BET66:BET66-T8-C2N* core (9:1) and *BET66-C4* shell. Amine-reactive AlexaFluor 532 NHS-ester channel is shown in blue, Cy5-maleimide is shown in red. Scale bars 50  $\mu\text{m}$ .

harvesting, where inter-layer interactions would be integral to achieving efficient device functionality. Acceptor photobleaching experiments revealed measurable interactions between FRET-pair fluorophores in two adjacent shell regions (**Figure 10, Table 3**). Because FRET interactions are highly dependent upon the intermolecular distance of the donor-acceptor pair—with 10 nm as the widely accepted limit for efficient FRET interaction—it is not unexpected that these experiments resulted in low efficiency measurements, with a highest calculated value of approximately 10%. The layer thickness of each shell is several microns, which puts most of the fluorophore guests in each layer outside of FRET distance with their designated FRET pair in the adjacent layer and allows

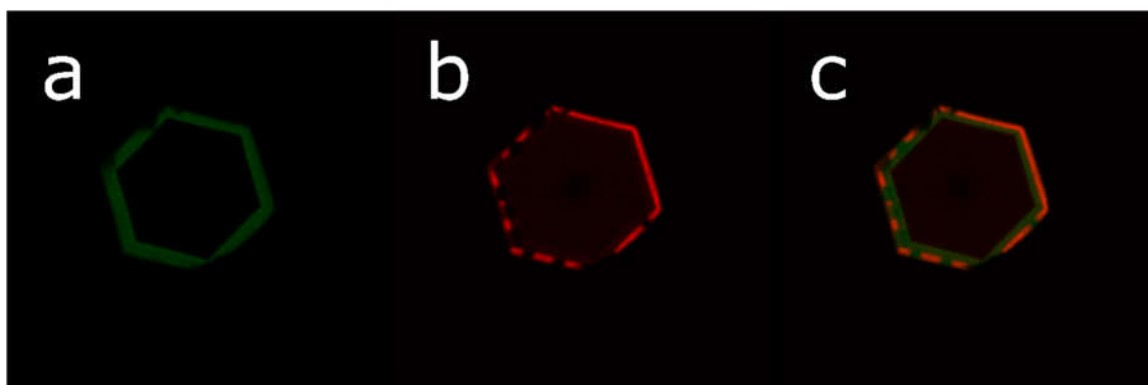


**Figure 10.** Acceptor photobleaching of multi-dye *BET66* crystal

(a) Donor channel—fluorescein. (b) Acceptor channel—DyLight 594—showing areas where acceptor fluorophores have been photobleached by high-intensity laser irradiation. (c) Overlay channel.

**Table 3.** Inter-layer FRET efficiency from acceptor photobleaching experiments

	Fluorescence (arb)				Average
	Region 1	Region 2	Region 3	Region 4	
Donor Pre-Bleach	<sup>a</sup> 27.55	33.49	32.57	28.83	
Donor Post-Bleach	28.95	35.15	36.11	29.78	
Acceptor Pre-Bleach	148.03	176.53	175.81	143.35	
Acceptor Post-Bleach	20.06	12.93	11.02	13.53	
FRET Efficiency	4.86 %	4.73 %	9.80 %	3.20 %	5.65 %

only the fluorophores very close to the layer interface to interact. In order to increase FRET efficiency of multi-layered crystals, each layer needs to be significantly finer, allowing all fluorophore guests to interact with FRET pairs in an adjacent layer. We predict that measuring these FRET interactions exclusively at the layer interface region would result in a much higher observed FRET efficiency, due to the proximity of interacting FRET pairs and exclusion of fluorophores which are outside of FRET range, although this experiment was beyond the scope of this proof-of-concept work. Assembly of multi-layered materials with guest molecules capable of interacting from layer to layer in this way can enable the

development of directionalized solid-state arrays which have the capability to physically constrain embedded processes. For example, light-harvesting arrays may use a FRET cascade to direct absorbed energy to a localized chemical storage moiety or multi-step solid-state catalysts may use directionality to increase their efficiency through physical separation of reactants, intermediates, and products. DNA structures have potential as effective materials for building customizable templates to organize directional arrays of fluorophores.<sup>63-65</sup>

This study employs fluorescent dyes to demonstrate for the first time that the BET66 crystal solvent channels allow for covalent post-crystallization conjugation of guest molecules. Although this study utilizes small molecule fluorophores to simplify visualization, there is potential for incorporation of a wide variety of guest molecules via pre- or post-crystallization conjugation, with the additional capability of layer-specific targeting of guest molecules for assembly of multifunctional solid-state DNA materials. The major limiting characteristics of potential guest molecule candidates would be size, hydrophobicity, and interactions with the DNA lattice which may interrupt the stability of the crystal structure.

### Chapter III –Microfluidics Approaches for *BET66* Crystal Growth and Labeling

Layer-by-layer crystal assembly via the standard crystallization drop method has several major limitations when considering production of crystals with specific tunable properties. The multiple washing steps which require physical handling of the crystals seem to increase the propensity for satellite crystal development, which can potentially disrupt the order of shell arrangement. In addition, the manual nature of this technique means that there are restrictions on the degree of control we have over the conditions. Understanding these factors, we chose to explore microfluidics approaches for layer-by-layer assembly in order to improve the levels of control, tunability, and automation in the assembly process (**Figure 11**). The potential advantages of a microfluidic system for

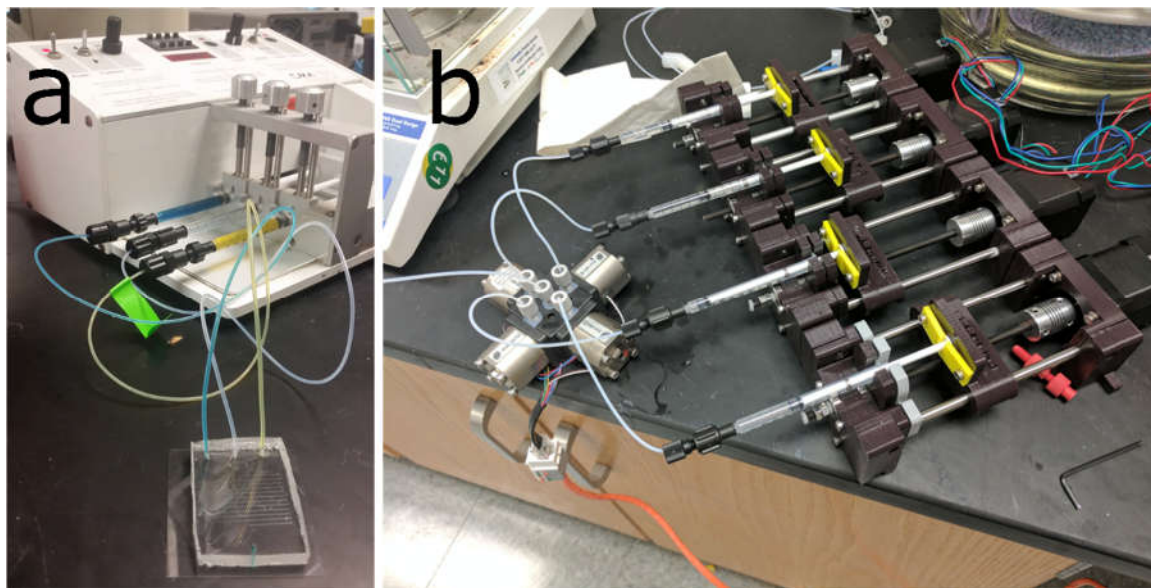


**Figure 11.** Microfluidics systems designed for in-line crystal growth

(a) A commercial multi-channel syringe pump capable of delivering three reagents to a microchannel simultaneously, pictured in-line with a glass-mounted polydimethylsiloxane microchannel. (b) Custom four-channel syringe pump, capable of delivering up to four reagents or up to three reagents with one channel withdrawing from the downstream end. This unit is controlled by a computer, which delivers complex sequences of instructions to each pump independently for automated core-shell growth procedures.

crystal assembly are many. Crucially, using an automated pumping system for delivery of reagents would allow all growth and washing steps to be completed in the same capillary without any need for manual intervention or physical handling of the crystals. A pre-programmed pumping system with in-line crystal growth would also increase repeatability of the methods and provide finer control over the protocol, to the sub-microliter scale, which would allow the properties of the crystals, specifically the shell layers, to be tuned as necessary.

For crystallization to occur, the environmental conditions around crystallization drops are equally important to the conditions and constituents within the drops. Typically, crystal growth relies on a concentration gradient within the crystal drop over time, which is driven by vapor diffusion from the drop to the surrounding buffer. An essential preliminary step to performing layer-by-layer assembly in a closed microfluidic system with no (or very limited) vapor diffusion was to show the capability of growing *BET66* crystals in this environment. We demonstrated successful crystal growth within glass-mounted polydimethylsiloxane (PDMS) microchannels (**Figure 12a**) and glass microcapillaries (**Figure 12b**), using standard *BET66*/Crystallization Buffer mixtures, and by simply injecting the mixture into a microchannel or capillary using a syringe pump. Crystals grown in this environment tended to be less than 50  $\mu\text{m}$  in their largest dimension, but were comparable to those grown in traditional crystallization drops.

The steps involved in core-shell crystallization require that reagents are added and washed out multiple times, which can be done easily in a microchannel, by pumping in new reagents and washing buffers at specific times. However, growing crystals in an

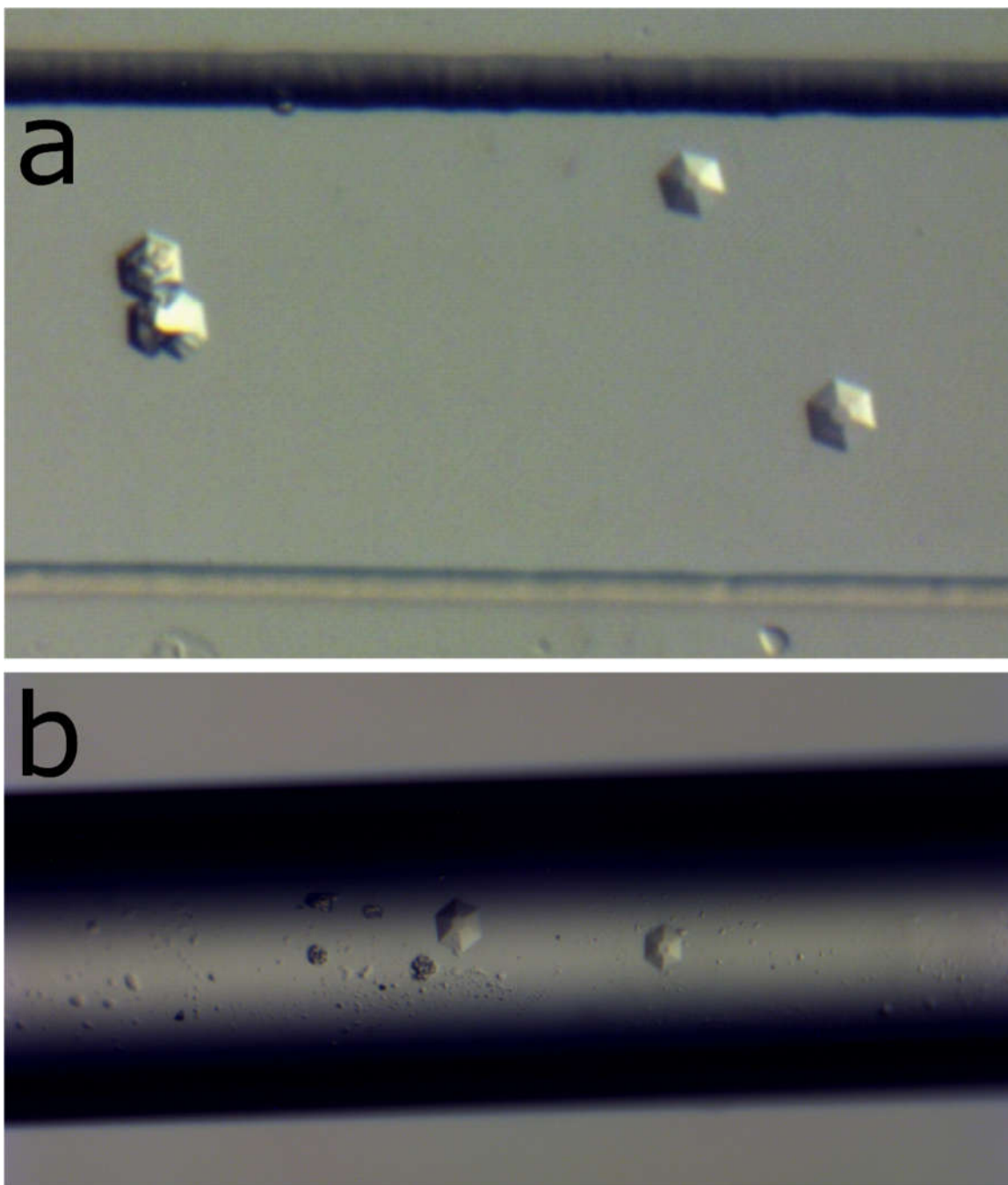


**Figure 12.** Crystals grown in microfluidics channels

Optical microscope images of *BET66* crystals grown in-line in (a) PDMS and (b) glass capillary microchannels. The crystals were grown in the standard buffer conditions.

environment which is under even a small amount of flow pressure introduces the potential for the crystals to be washed out of the system. We found that in order to reliably prevent this, flow rates needed to be kept in the range of 0.2-0.5  $\mu\text{L}/\text{min}$  after the initial crystal growth step. Flow rates in this range allowed us to perform washing steps with Crystallization Buffer and introduce additional reagents for shell growth without noticeably disturbing the existing crystals.

To produce crystal cores, *BET66* and Crystallization Buffer were injected into PDMS microchannels or glass capillaries. A thorough wash was performed by pumping through excess Crystallization Buffer, and then the shell mixture of buffer and *BET66:BET66-Fluor* (49:1) was slowly injected and allowed to incubate and form the shell. The crystals were examined by confocal microscopy by placing the entire channel onto the stage, to eliminate the need for removing them from the channels, which would risk destruction or degradation of the crystals. Confocal microscopy showed successful assembly of the fluorescent shell, completely surrounding the core crystals (**Figure 13**).

Initial experiments were performed by manually loading syringes containing the necessary reagents into pumps, setting the flow rate, and waiting a prescribed amount of time. In order to further streamline the multi-step process and eliminate the need for changing syringes part of the way through, a computer-controlled multi-channel syringe pump was implemented. By loading an appropriate script into the controller, a multi-step process can be performed end-to-end with no human intervention. The script directs the controller to inject up to three reagents simultaneously—at independent flow rates—and to hold for specific time intervals for incubation. This allows, for example, core DNA

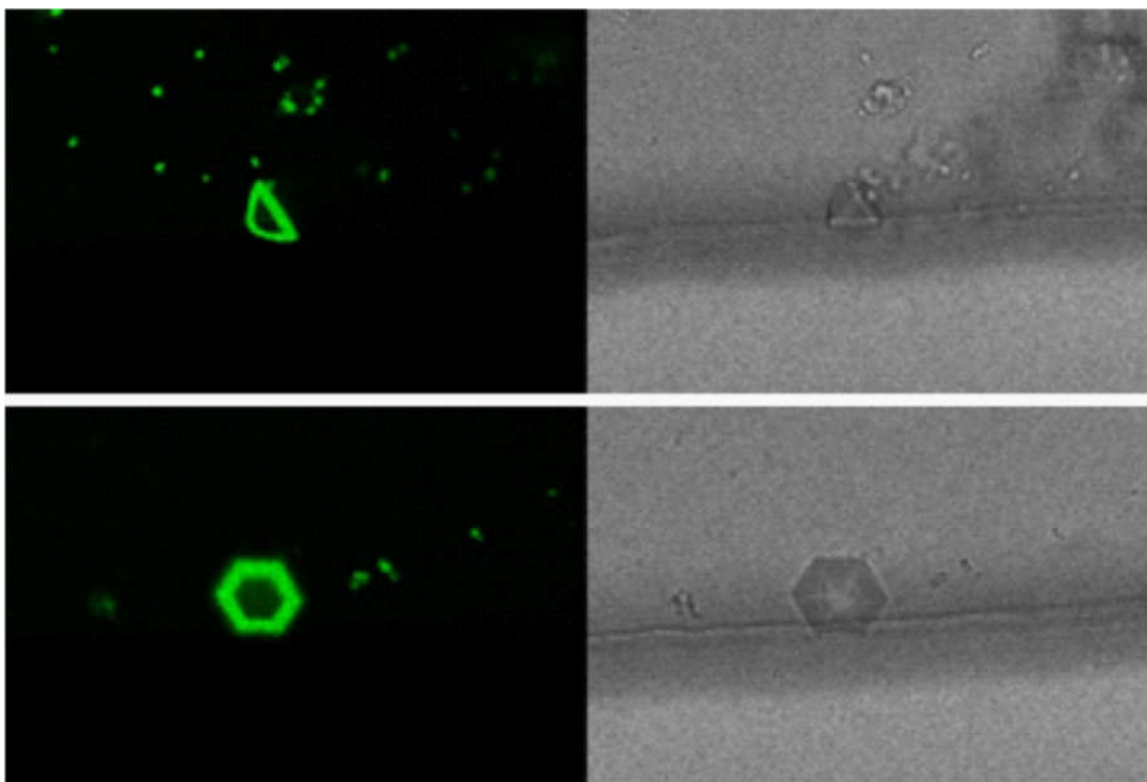


**Figure 13.** In-line core-shell assembly of crystals in a microfluidics channel

Confocal microscope images of two core-shell *BET66* crystals grown in-line in a microchannel. The *BET66*:*BET66-Fluor* (49:1) shells fully encapsulate the *BET66* core crystals. Images of the crystals are shown perpendicular (top) and parallel (bottom) to the six-fold symmetry axis. Fluorescein emission (left) and bright field (right) channels are shown for each crystal.

solution, shell DNA solution, and Crystallization Buffer to be loaded into separate syringes and a full core-shell assembly protocol to be completed automatically.

We have demonstrated proof-of-concept for the use of microfluidics systems in core-shell crystallization of functionalized oligonucleotide crystals. This has distinct advantages over the traditional crystallization drop format, including the elimination of physical handling of crystals and the ability to automate each step in the process, thereby decreasing the human factor and increasing reproducibility. This method could also potentially be scaled up to increase throughput. The computer-controlled injection system gives a high degree of control over the volume, flow rate, and mixing ratio at each step, and offers the potential for finely tuned layer-by-layer assembly and labeling properties, which can be easily changed from trial to trial once calibrated.

## Chapter IV – Exploring Growth of *BET66* Nanocrystals and Visualization of the Crystal Lattice by Electron Microscopy

The *BET66* crystals we have demonstrated here are typically within the range of 50-150  $\mu\text{m}$  corner-to-corner of the large hexagonal base. However, some of the target applications require much smaller size constraints. For example, nanoparticles designed for drug delivery are typically between 10 and 1000 nm, with many examples falling in the range of 50-100 nm.<sup>66,67</sup> In the interest of designing the *BET66* system to fulfill the requirements of diverse applications, we began efforts to investigate whether our crystals could be reproducibly grown in this size range, by altering the crystallization conditions.

Transmission electron microscopy was chosen as the method for analyzing crystals in these experiments. Transfer of crystals onto TEM grids after growth may have proved problematic, due to the target size range being significantly smaller than any nylon crystal loops available. To eliminate the need for this, a sitting drop setup for crystallization was devised in which the drop was placed directly on a TEM grid. *BET66* crystals were found by optical microscopy to grow readily on the TEM grids (not shown). After negative staining with uranyl acetate, the grids were examined by TEM for evidence of intact crystals. Hexagonal objects were observed, which were analogous to the *BET66* crystal morphology looking parallel to the six-fold symmetry axis (**Figure 14**). Examined at higher magnification, these objects consistently displayed an internal hexagonal grid pattern (**Figure 15a**) with a grid size similar to that of the *BET66* crystal unit cell measurement from the Protein Data Bank entry (PDB: 1P1Y).<sup>49</sup> The measured unit cell from TEM was 35.16  $\text{\AA}$ , compared to a value of 40.63  $\text{\AA}$  from the crystal structure. The decrease in size can be accounted for in the drying of the crystals necessary for TEM

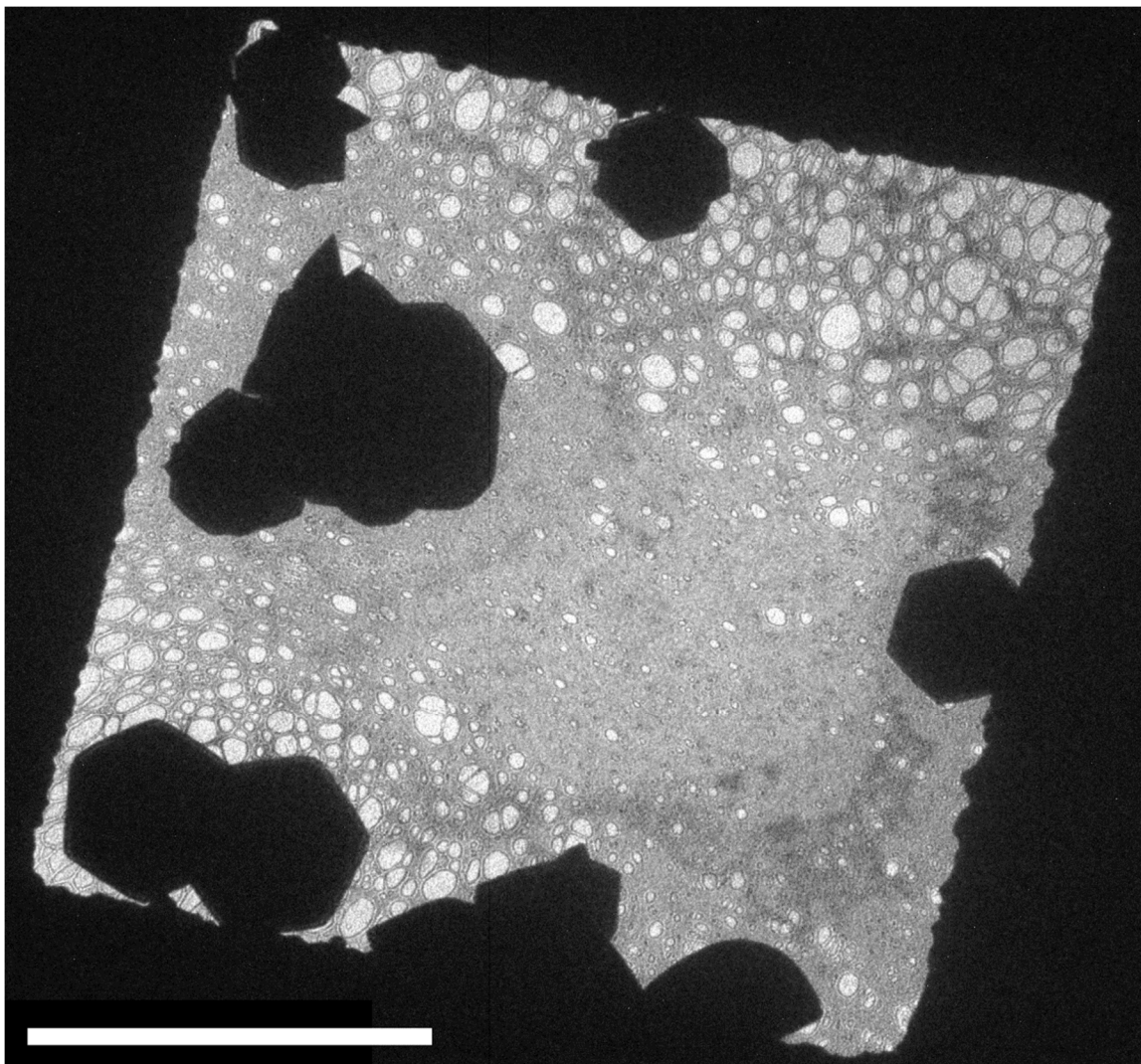


**Figure 14.** TEM images of *BET66* crystals grown on TEM grids

TEM images of *BET66* crystals grown on-grid and stained with uranyl acetate, recognizable by their characteristic hexagonal outline. The crystals on the pictured grid sector range from approximately 5 to 10  $\mu\text{m}$ . Scale bar 20  $\mu\text{m}$ .

preparation, which likely reduces their volume by a significant amount. Interestingly, the measured size of the solvent channels from the TEM images was approximately the same as the size calculated from the crystal structure (**Figure 15b**)—19.69 Å and 19.54 Å, respectively. Electron diffraction performed using the TEM showed a hexagonal diffraction pattern (**Figure 15c**), which is characteristic of the six-fold symmetry of a *BET66* crystal. The unit cells were measured from TEM images captured and the data were comparable to the X-ray diffraction data. We found that, due to the unipyramidal morphology of *BET66* crystals, the crystal lattice was most clearly visible near the edges of the crystal, as the sample thickness increases toward the center. A 5'-truncated *BET66* variant (*BET66-Δ5'*) has been previously demonstrated as a crystal habit modifier, which alters the crystal morphology from hexagonal pyramidal to thinner hexagonal tabular, based on the ratio of the habit modifier to the standard *BET66*.<sup>61</sup> Crystals of *BET66-Δ5':BET66* (1:49) were grown on-grid and stained with uranyl acetate as described. Due to the decreased sample thickness, the hexagonal lattice pattern was clearly visible throughout a much larger portion of these crystals (**Figure 16**). These crystals were still larger than the target size of 10-1000 nm, however.

Variations of the Crystallization Buffer containing higher magnesium concentrations are known to increase the number of crystals in a given crystallization drop while simultaneously decreasing their size. This is thought to be primarily due to an increased number of nucleation events resulting from the higher magnesium concentration. We took advantage of this correlation to attempt to scale down the growth size of *BET66* crystals by simply altering the buffer concentrations. Crystal drops plated on-grid with 240, 360, and 480 mM magnesium-containing TEM Crystallization Buffers reliably

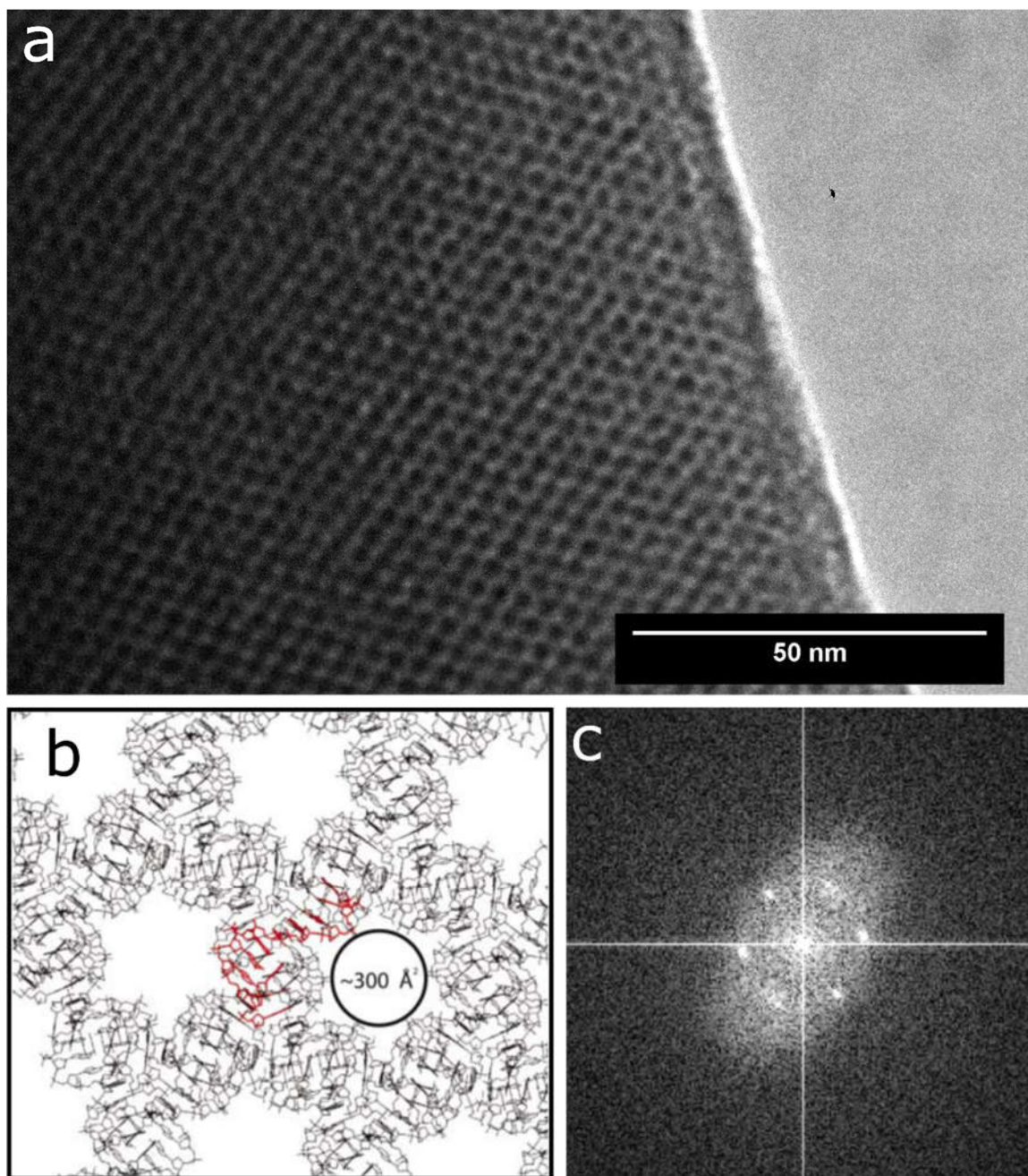


**Figure 15.** Crystal lattice of *BET66* shown through TEM

(a) A *BET66* crystal shown at 200kx magnification. The light gray hexagonal DNA lattice is with the solvent channels as periodic dark spots, as a result of absorbing uranyl acetate during staining. (b) The structure of the *BET66* crystal lattice, looking down the six-fold symmetry axis. Each solvent channel has approximately a  $300 \text{ \AA}^2$  cross-sectional area, giving a diameter of  $\sim 19.54 \text{ \AA}$  (Figure from Paukstelis, et al., 2004). (c) Electron diffraction gives a hexagonal pattern of diffraction spots, characteristic of the *BET66* crystal lattice.



**Figure 16.** TEM image of a *BET66-Δ5':BET66* (1:49) crystal

The addition of the 5'-truncated nucleic acid results in crystals with a hexagonal tabular morphology which are thinner in the z dimension. The lattice structure in these crystals is widely visible over a large portion of the crystal when imaged with TEM, due to the decreased sample thickness.

produced *BET66* crystals with smaller minimum sizes, though the size distribution on a given grid was relatively wide (Selected images shown in **Appendix D**), leaving room for improvement of the consistency and reproducibility of the crystals. The smallest crystals produced in these studies were approximately 500 nm, which is within the target range of 10-1000 nm (**Figure 17**).

A second habit modifier, *BET66-Δ3'*, is a 3'-truncated variant of *BET66*. Independently, these habit modifiers change the morphology of the *BET66* crystals by effectively slowing the rate of growth either parallel to or perpendicular to the six-fold

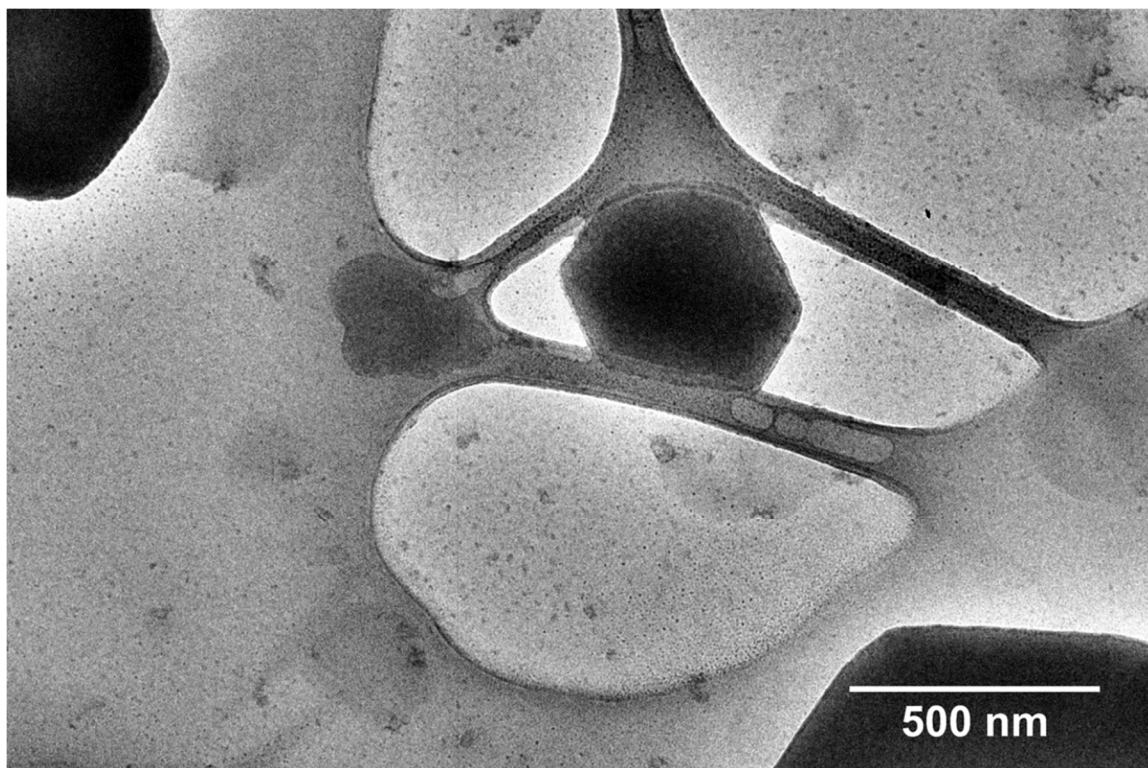


**Figure 17.** TEM image of a *BET66* nanocrystal

The smallest *BET66* crystal produced in this study measured approximately 500 nm corner-to-corner. This crystal was generated using a 1:1 mixture of 400  $\mu\text{M}$  DNA and Crystallization Buffer with 360 mM magnesium formate and 20% 2-methyl-2,4-pentenediol (MPD), crystallized on-grid and stained with 0.2% uranyl acetate.

symmetry axis. Crystallization of *BET66* in the presence of *BET66- $\Delta$ 5'* produces crystals of a hexagonal tabular morphology, while the presence of *BET66- $\Delta$ 3'* produces crystals of a hexagonal columnar morphology. We reasoned that, if both habit modifiers were combined in appropriate ratios with *BET66*, the overall growth rate of the crystal could be limited and this would result in smaller crystal size, and potentially a narrower size distribution. To accomplish this, crystals were plated in sitting drops using various ratios of *BET66- $\Delta$ 5'*:*BET66- $\Delta$ 3'*:*BET66* to determine an appropriate ratio for consistent crystal growth. After a number of trials, a mixture of 2:25:73 *BET66- $\Delta$ 5'*:*BET66- $\Delta$ 3'*:*BET66* was

found to produce crystals close to the original hexagonal pyramidal morphology. In order to further stabilize crystals to the addition of uranyl acetate and the drying necessary for TEM preparation, we used a crosslinking procedure which was previously demonstrated to stabilize *BET66* crystals to significantly decreased magnesium concentrations and increased temperatures.<sup>68</sup> The *BET66-Δ5'*:*BET66-Δ3'*:*BET66* crystals grew readily on the TEM grids (**Figure 18a**), although we noticed that the hexagonal lattice pattern was much fainter (**Figure 18b**). This suggests that the combination of both habit modifiers and the TEM preparatory protocol may weaken the crystal structure to some degree, despite the presence of the crosslinker, which is meant to tether the DNA molecules within the crystal together, but does not necessarily promote the typical crystal lattice contacts.

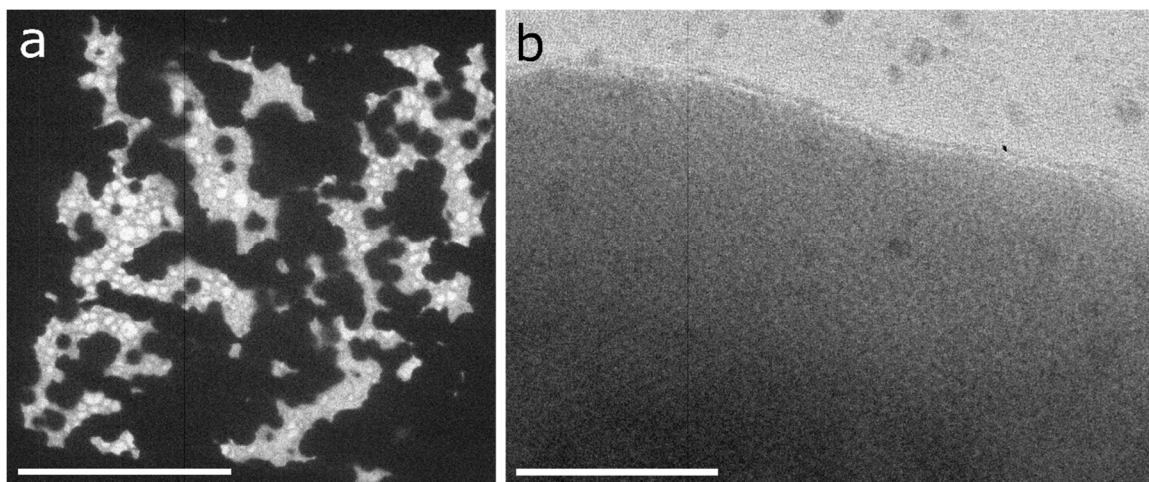


**Figure 18.** TEM images of crosslinked *BET66* crystals

(a) TEM image of *BET66* crystals grown on-grid, crosslinked using bis(2-chloroethyl)amine, and stained with uranyl acetate. Scale bar 20  $\mu\text{m}$ . (b) A crosslinked crystal viewed at 200kx magnification. The hexagonal lattice pattern is discernable, but much weaker than typically observed in crystals which were not crosslinked. Scale bar 50  $\mu\text{m}$ .

There is space for improvement of the consistency, as the crystals produced in these experiments fell on a size distribution and many of the crystals grew larger than the maximum desired size of 1000 nm. We have conceived of several techniques in addition to those presented here, which we believe to have potential in reaching this goal. There is a trend across sitting drops of *BET66* that drops of larger volume tend to produce larger crystals than smaller volume drops plated using otherwise identical conditions. Drastically decreasing the size of crystal drops by depositing the mixture as an aerosol may produce significantly smaller crystals. In addition, we predict that crystal size could be decreased by limiting the incubation time, which could be achieved by diluting the drops with Crystallization Buffer after a prescribed growth period. A combination of these or other techniques may be necessary to produce consistently sized nanocrystals, although preliminary experiments have not yielded meaningful trends.

Here, we have shown the first TEM images of *BET66* crystals, which provides a unique visual representation of the internal lattice structure not obtainable by X-ray diffraction. We have also demonstrated the capability to grow *BET66* as nanocrystals on the scale of hundreds of nanometers, which is approximately two to three orders of magnitude smaller than is typically produced. We have used the very simple technique of varying the buffer conditions, particularly the magnesium concentration, to produce crystals on this scale. We predict that the techniques discussed here, including the use of crystal habit modifiers and specific crystallization conditions have the potential to generate consistent and reproducible *BET66* nanocrystals. This achievement would enable the use of the *BET66* crystal lattice as a biomaterial scaffold in nanoscale applications, such as drug delivery.

## Conclusions

*Some contents of this chapter are adapted from McNeil, R. & Paukstelis, P. J. Core-Shell and Layer-by-Layer Assembly of 3D DNA Crystals. Adv. Mater. 29, 1701019 (2017).*

*BET66* has unique crystallization properties which allow it to undergo isothermal core-shell assembly. This is distinct from other 3D DNA crystals, many of which require annealing steps for efficient formation of lattice contacts for crystal assembly.<sup>7,69</sup> Isothermal growth of *BET66* crystals is related to the noncanonical base pairs, which are involved in directing the anisotropic growth of the crystals down the six-fold symmetry axis and influencing the morphology of these crystals. Based on evidence from shell growth studies, this anisotropic character is present in shell growth as well, indicating that the crystallization mechanism is the same or very similar to that of initial crystal formation. Evidence from previous work suggests that the formation of the noncanonical base pairs occurs after that of the Watson-Crick base pairs.<sup>50</sup> These findings together suggest that noncanonical base pairs may have advantages in their ability to form strong lattice contacts upon incorporation into the crystal but not prior to it. There is increasing appreciation for the importance forming weak lattice contacts pre-incorporation in terms of productive DNA crystal assembly.<sup>30,69,70</sup>

In this study, we demonstrate for the first time that the solvent channels of *BET66* crystals allow sufficient volume for covalent post-crystallization modification using small molecule fluorophores. Although the scope of this study was limited to fluorescent dyes, a wide assortment of guest molecules including peptides or catalytic moieties could be incorporated using the pre- and post-crystallization methods described here. The primary limitations on guest molecule incorporation would be the size and shape, which would limit

the ability to fit within the volume of the solvent channels, and their compatibility with the DNA lattice—molecules which form interactions with the DNA that may disrupt crystal contacts.

Further, we have demonstrated the ability to address guest molecules to specific layers of core-shell crystals. This showcases the potential of these crystals for the design of multifunctional materials through using stepwise layer-by-layer or orthogonal labeling approaches. Due to the nature of the DNA lattice, guest molecules can be placed periodically with Ångstrom-level precision within the desired crystal layer. Though the position on the *BET66* sequence can be specified, the absolute position in space depends to an extent on the flexibility of the linker used.<sup>65,71,72</sup> There is no requirement for the attachment location or method to be identical in each layer, so a variety of techniques could be employed to achieve precise placement of guest molecules in the periodic scaffold, down to specific spatial orientation. In addition to this, our results suggest that the properties of individual crystal layers, including layer thickness, can be tuned through varying the growth conditions and incubation time. This method provides a new approach for creating multifunctional solid-state biomaterials with tunable chemical and physical properties.

We have shown proof-of-concept for performing core-shell crystal assembly using microfluidics systems. We successfully overcame the challenge of translating a technique typically relying on vapor diffusion properties for crystal growth to a medium which minimizes the possibility of this phenomenon to occur. This technique has distinct advantages over traditional crystal drops, including minimal physical handling of the crystals, higher throughput, and finer tunability via computer control. Microfluidics allows

us to assemble core-shell crystals from end-to-end with no human intervention, setting the stage for automated and reproducible assembly of multifunctional biomaterials using *BET66*.

Finally, the TEM images from this study have expanded our understanding of the *BET66* crystals by providing a visual representation of the lattice structure and solvent channels not previously obtained through X-ray crystallography. Additionally, we demonstrated successful growth of *BET66* nanocrystals through simply changing the growth and buffer condition. Typical *BET66* crystals grown in sitting drops fall within the range of 50-150  $\mu\text{m}$ . We successfully generated crystals in the range of 500-1000 nm—approximately two orders of magnitude smaller and the first nanoscale *BET66* crystals observed. This introduces new avenues for use of *BET66* crystals in applications requiring customizable nanoscale materials, such as drug delivery. *BET66* crystals are a promising platform for the design of highly customizable multi-layered and multifunctional biomaterials for micro- and nanoscale applications, such as light harvesting, drug delivery, and solid-state catalysis.

## Methods

### *Oligonucleotide Synthesis and Purification*

DNA oligonucleotides were synthesized (DMT-off) using an Expedite 8090 synthesizer (Perseptive Biosystems, Foster City, CA). Reagents and phosphoramidite monomers for synthesis were purchased from Glen Research (Sterling, VA). An aqueous solution of 30% ammonium hydroxide was used for one-step cleavage and deprotection of *BET66*, *BET66-Fluor* (3'-fluorescein-modified variant), and *BET66-T8-C2N* (5-amino-dT-substituted variant) oligonucleotides. *BET66-C4-SH* was cleaved and deprotected using a mixture of 1:1 water and cystamine free base as described by MacMillan and Verdine.<sup>73</sup> Following cleavage and deprotection, crude oligonucleotides were separated via a denaturing 20% polyacrylamide gel (19:1 acrylamide:bis-acrylamide) to remove truncated products. The full-length oligonucleotides were removed from the gel by electroelution, precipitated in ethanol, redissolved in water, and dialyzed to remove small molecule (>1 kD) impurities. The crystal habit modifiers *BET66-Δ5'* and *BET66-Δ3'*, with sequences d(CAG CTG GGA G) and d(GGA CAG CTG) respectively, were obtained from Diana Zhang.<sup>61</sup>

### *Crystallization*

*BET66* (and variant oligonucleotide) crystals were grown by mixing small volumes of oligonucleotide solution and Crystallization Buffer as sitting drops. The standard buffer used for these experiments is composed of 120 mM magnesium formate, 50 mM lithium chloride, and 10% 2-methyl-2,4-pentanediol (MPD). A typical crystal drop was composed of 4 μL of 200 μM oligonucleotide solution and 4 μL of Crystallization Buffer. However, depending on the specific batch of oligonucleotide and the application, the volume of each

component and the concentrations of oligonucleotide and buffer components varied. Generally, the volumes of oligonucleotide and buffer fell between 1  $\mu\text{L}$  and 4  $\mu\text{L}$  with typical DNA:buffer ratios of 2:1, 1:1, or 1:2 and the most common concentration ranges for each component was 100-400  $\mu\text{M}$  oligonucleotide, 120-240 mM magnesium formate, 50-100 mM lithium chloride, and 10-20% MPD. Well solution for crystal drops was matched to the initial buffer used to mix the drop. Crystal plates were covered and incubated overnight at 22° C. *BET66-C4-SH* crystals were grown either using the method described in this section or as a mixture of *BET66* and *BET66-C4-SH* at 9:1. Due to the size of the attached fluorescein group and the additional crowding it introduces, crystals *BET66-Fluor* were grown as a mixture of *BET66* and *BET66-Fluor* at 9:1 or 49:1.

#### *Core-Shell and Layer-By-Layer Crystal Assembly*

*BET66* crystals to be used as cores were washed at least five times by the addition and removal of 20  $\mu\text{L}$  of Crystallization Buffer to remove excess DNA remaining in solution after the crystallization process. The crystal cores were then transferred to a fresh crystal drop containing 2  $\mu\text{L}$  of Crystallization Buffer and 2  $\mu\text{L}$  of the desired shell DNA solution—typically either *BET66:BET66-Fluor* (9:1 or 49:1) or *BET66-C4-SH*—100  $\mu\text{M}$  final concentration. The drops were then incubated overnight at 22° C to allow development of the shell layer.

Layer-by-layer assembly was done using the same method, repeated for multiple iterations. The washing step was performed between each of the shell growth stages to prevent residual DNA from the previous step from incorporating into the subsequent layer. Layer assembly steps for multi-layered crystals were incubated at 22° C for between two hours and overnight, depending on the desired layer thickness.

### *Confocal Fluorescence Microscopy*

To prepare crystals for imaging, a final washing step was performed to remove all noncrystallized DNA and any excess reagents from labeling steps. This washing step was performed as described in the previous section. Crystals were transferred to a drop in a recessed microscope dish, which was then sealed with a cover slip to prevent evaporation and drying of the crystals. Imaging was performed using a Leica SP5X confocal fluorescence microscope. Z-axis scans were taken by capturing images in 1  $\mu\text{m}$  slices. See **Table 4** for excitation and emission wavelengths used to visualize each fluorophore. Image analysis was done using the Leica Application Suite Advanced Fluorescence software and FIJI (ImageJ).

**Table 4.** Excitation/emission wavelengths used for fluorophore visualization

	Excitation Wavelength (nm)	Emission Wavelength Range (nm)
Fluorescein	490	505-565
Cy5	631	650-750
AlexaFluor 532	532	544-584
DyLight 594	593	5930-720

### *Shell Growth Kinetics*

Crystal cores were washed and prepared for shell growth/confocal microscopy as previously described. Crystals were placed into a 6  $\mu\text{L}$  drop of Crystallization Buffer on a recessed microscope dish and positioned with the six-fold symmetry axis parallel to the light path of the microscope using a nylon loop. 3  $\mu\text{L}$  of the shell DNA solution of 49:1 *BET66:BET66-Fluor* was added to the dish at a final concentration of 200  $\mu\text{M}$ . Z-axis scans were recorded through the entire crystal in 1  $\mu\text{m}$  slices. At each time point and each Z-stack image, the shell width was calculated from the average of twelve measurements

(two on each of the six sides of the crystal). Base thickness was calculated from the average of eight measurements from eight different positions across the (001) crystal face. Measurements were made using an image analysis script written by the authors and run using FIJI (ImageJ) software (**Appendix E**). In summary, a fluorescence threshold was applied to each image, and the software collected measurements by calculating the distance between the pixel on each edge of the fluorescent shell, or base.

#### *Post-Crystallization Labeling*

Conjugation reactions of dye maleimides to crystals containing *BET66-C4-SH* were performed in Labeling Buffer (composed of 120 mM magnesium formate, 50 mM lithium chloride, 10% 2-methyl-2,4-pentanediol, and 25 mM 4-(2-hydroxyethyl)-1-piperazineethanesulfonic acid (HEPES) at pH 7.2), 50 mM TCEP, 1 mM maleimide dye, and 10% dimethylformamide (DMF) in water. Dye maleimides used for these experiments included fluorescein-5-maleimide, Cy5-maleimide, and DyLight 594-maleimide. Orthogonal labeling of crystals containing both *BET66-T8-C2N* and *BET66-C4-SH* with NHS-ester and maleimide dyes was done in identical reaction conditions, but at pH 7.5. AlexaFluor 532-NHS-ester was used for these experiments. Crystals were washed with fresh Crystallization Buffer after labeling and before analysis to remove excess reagents from the reaction.

#### *Quantitation of In-Crystallo Labeling*

Quantitation of *in crystallo* thiol-maleimide conjugation reactions was done by <sup>32</sup>P radiolabeling. Crystals were washed, dissolved in 4 μL of water, and radiolabeled with <sup>32</sup>P by way of 25 μCi [ $\gamma$ -<sup>32</sup>P]-ATP (Perkin-Elmer, Waltham, MA) using T4 polynucleotide kinase (New England Biolabs, Ipswich, MA) following the manufacturers' recommended

procedures. Radiolabeled samples were analyzed via separation on a denaturing 20% polyacrylamide gel (19:1 acrylamide:bis-acrylamide), exposure on a storage phosphor screen, and quantitation using a phosphorimager.

#### *FRET Acceptor Photobleaching*

Photobleaching experiments were done using the FRET pair fluorescein (donor) and DyLight 594 (acceptor) on a Leica SP5X confocal fluorescence microscope, using the included software tool for performing FRET acceptor photobleaching experiments. Donor and acceptor fluorescence were measured before and after photobleaching of the acceptor by high-intensity laser irradiation using the excitation wavelength. FRET efficiency was calculated from these measurements by the software, applying correction factors for donor/acceptor channel crosstalk obtained from control samples.

#### *Microcapillary Crystallization and Labeling*

Microcapillary crystallization was done using a multi-channel syringe pump setup of original design. Oligonucleotide solution, Crystallization Buffer, and labeling reagents were loaded into syringes separately. A prewritten method file coordinated pumping from the syringes and opening/closing of the solenoid valves to deliver the desired mixture of components to the glass microcapillary. For *de novo* crystallization, oligonucleotide solution and Crystallization Buffer were delivered at 10  $\mu\text{L}/\text{min}$  each and incubated overnight with zero flow rate to allow crystal growth. For shell growth and labeling steps, appropriate reagents were delivered at combined flow rates of 0.2-0.5  $\mu\text{L}/\text{min}$  to avoid washing the existing crystals out of the capillary. In all cases, the total volume delivered was at least one and a half times the system volume estimated based on the length and inner

diameter of the capillary and each tubing section. Volume delivered for washing steps was ten times the estimated system volume, to ensure thorough removal of excess reagents.

### *Transmission Electron Microscopy*

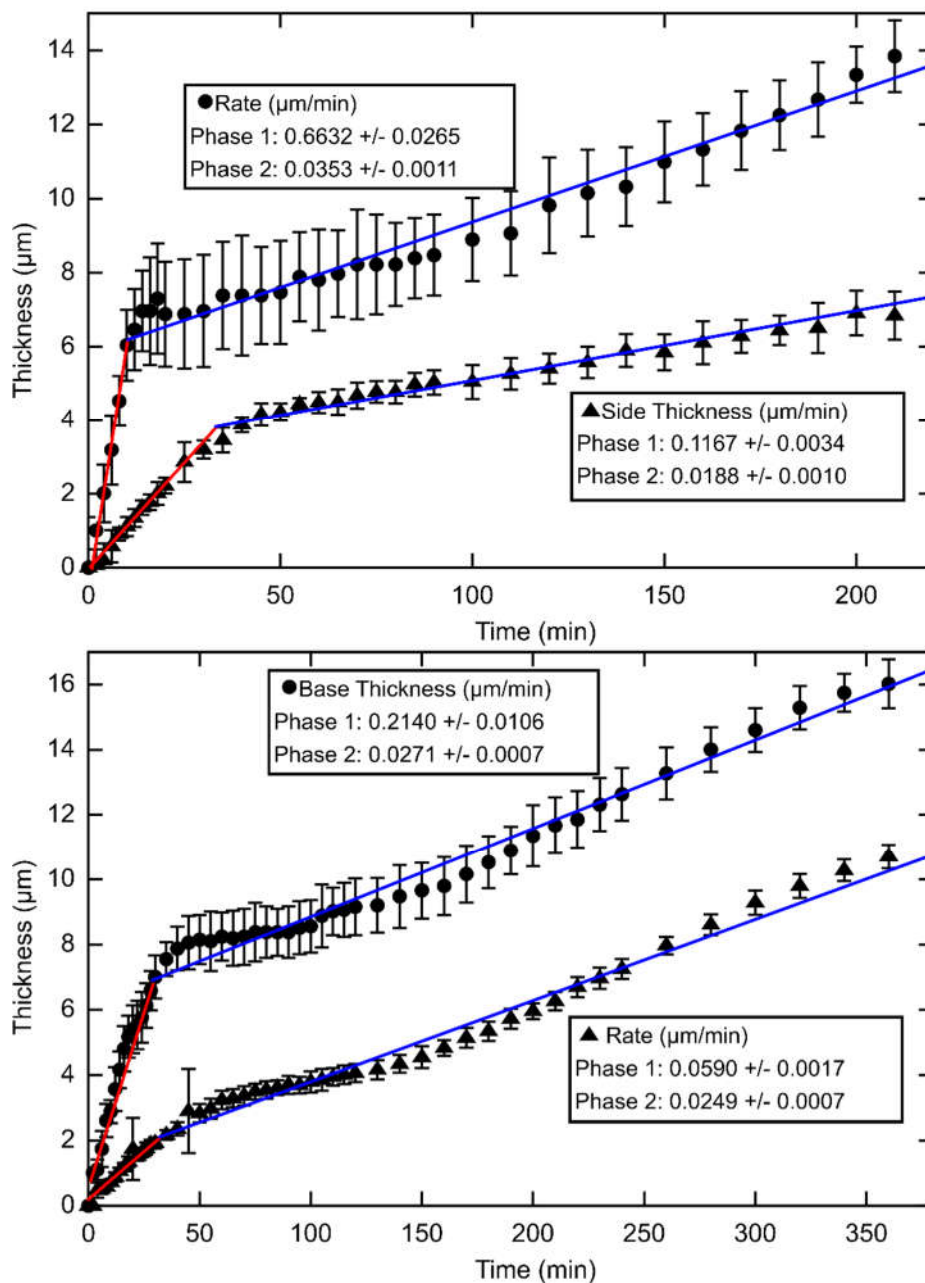
Crystals for TEM analysis were grown in sitting drops directly on TEM grids—400 mesh copper grids with ultrathin carbon film on lacey carbon support (Ted Pella, Inc., Redding, CA). 1.5  $\mu\text{L}$  of 200  $\mu\text{M}$  *BET66* was mixed with 1.5  $\mu\text{L}$  of Crystallization Buffer on-grid, Crystallization Buffer was added to the wells, and the drops were sealed and incubated overnight at 22° C. After crystal growth, 2  $\mu\text{L}$  of solution was removed and the TEM grids were washed by addition and subsequent removal of 2  $\mu\text{L}$  of Crystallization Buffer. Samples were negatively stained by addition of 2  $\mu\text{L}$  of 0.2% aqueous uranyl acetate solution for five minutes. Finally, 2  $\mu\text{L}$  was removed, grids were washed as before with 2  $\mu\text{L}$  of Crystallization Buffer, and allowed to air dry for at least thirty minutes. on a JEOL JEM 2100 transmission electron microscope with a lanthanum hexaboride ( $\text{LaB}_6$ ) electron source.

Where indicated, special TEM Crystallization Buffers were substituted for the standard buffer. The concentration of magnesium formate and MPD were varied in these buffers—from 120 to 480 mM and from 10 to 30%, respectively. In addition, higher concentration DNA solutions were used in certain experiments, ranging from the standard 200  $\mu\text{M}$  up to 400  $\mu\text{M}$ . Crystals grown with *BET66- $\Delta$ 5'* crystal habit modifiers used a ratio of 1:49 *BET66- $\Delta$ 5'*:*BET66* at the standard 200  $\mu\text{M}$  total oligonucleotide concentration. Crystals grown with both *BET66- $\Delta$ 5'* and *BET66- $\Delta$ 3'* crystal habit modifiers used a ratio of 2:25:73 *BET66- $\Delta$ 5'*:*BET66- $\Delta$ 3'*:*BET66*.

Crosslinking of crystals for TEM was done using bis(2-chloroethyl)amine, a DNA alkylating agent. The crosslinker was deposited onto crystal drops at a final concentration of 1 mg/mL and allowed to incubate at 4° C overnight. The drops were then washed thoroughly with Crystallization Buffer and the overnight crosslinking procedure was repeated as described. After crosslinking, a final wash with Crystallization buffer was done before staining and preparation for TEM.

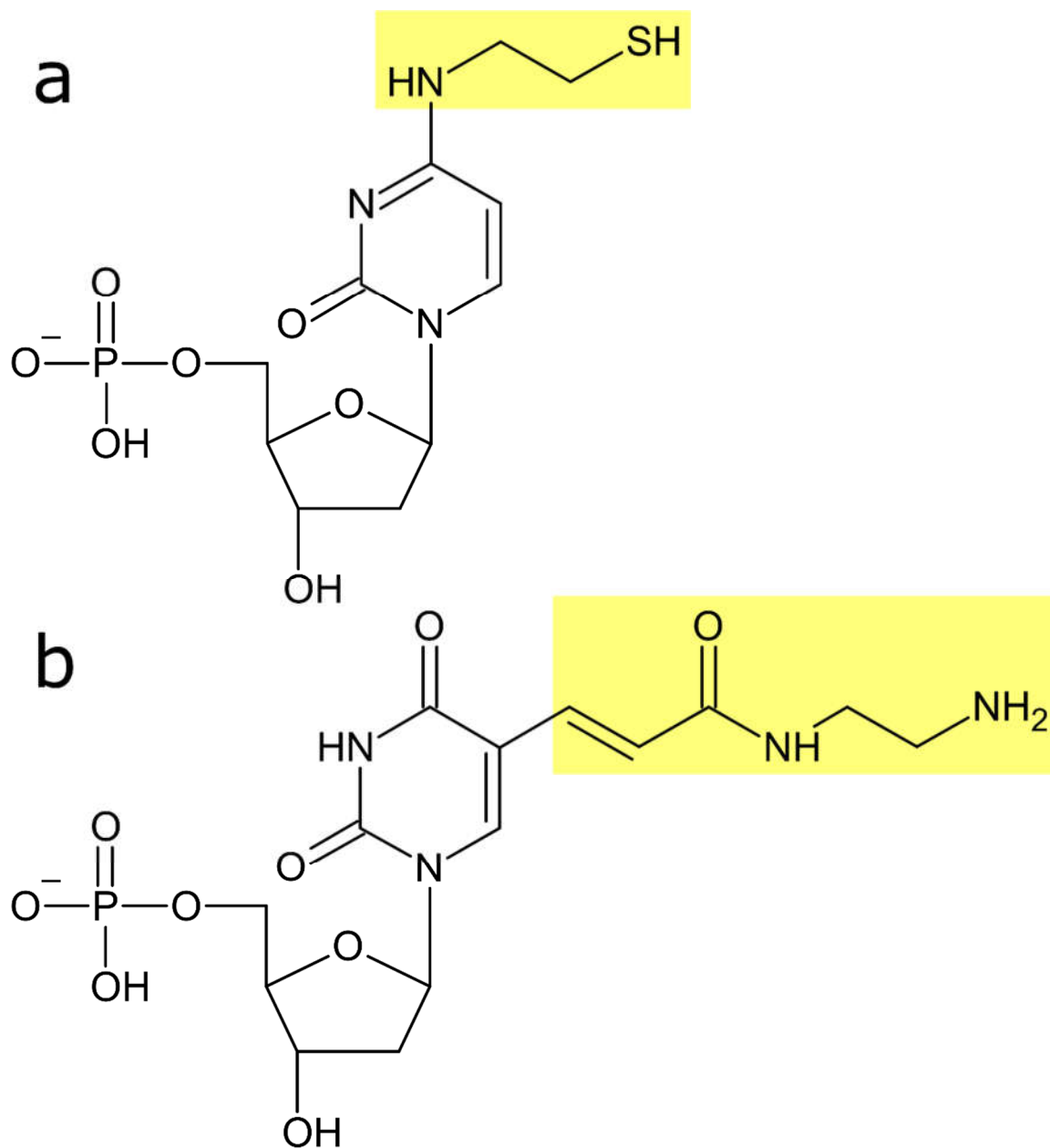
## Appendices

### Appendix A – Supplemental Shell Growth Kinetics Data



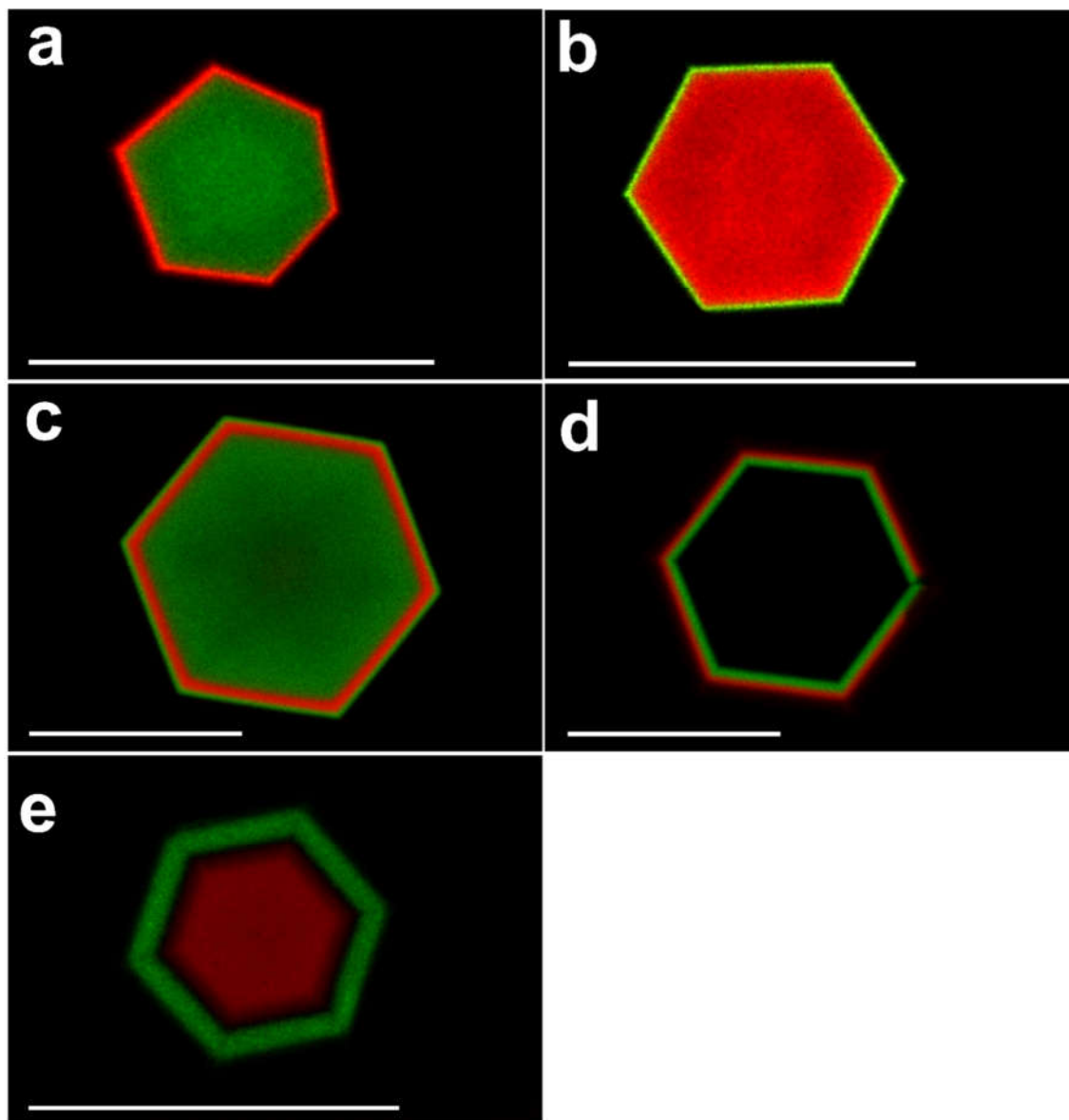
Time-resolved measurements of shell thickness on the base and sides of two additional *BET66* crystals to supplement Figure 2. Best fit lines for each phase are shown, and corresponding rate values are listed in the legends.

Appendix B – Structures of Modified Nucleotides Used for Guest Molecule Coupling



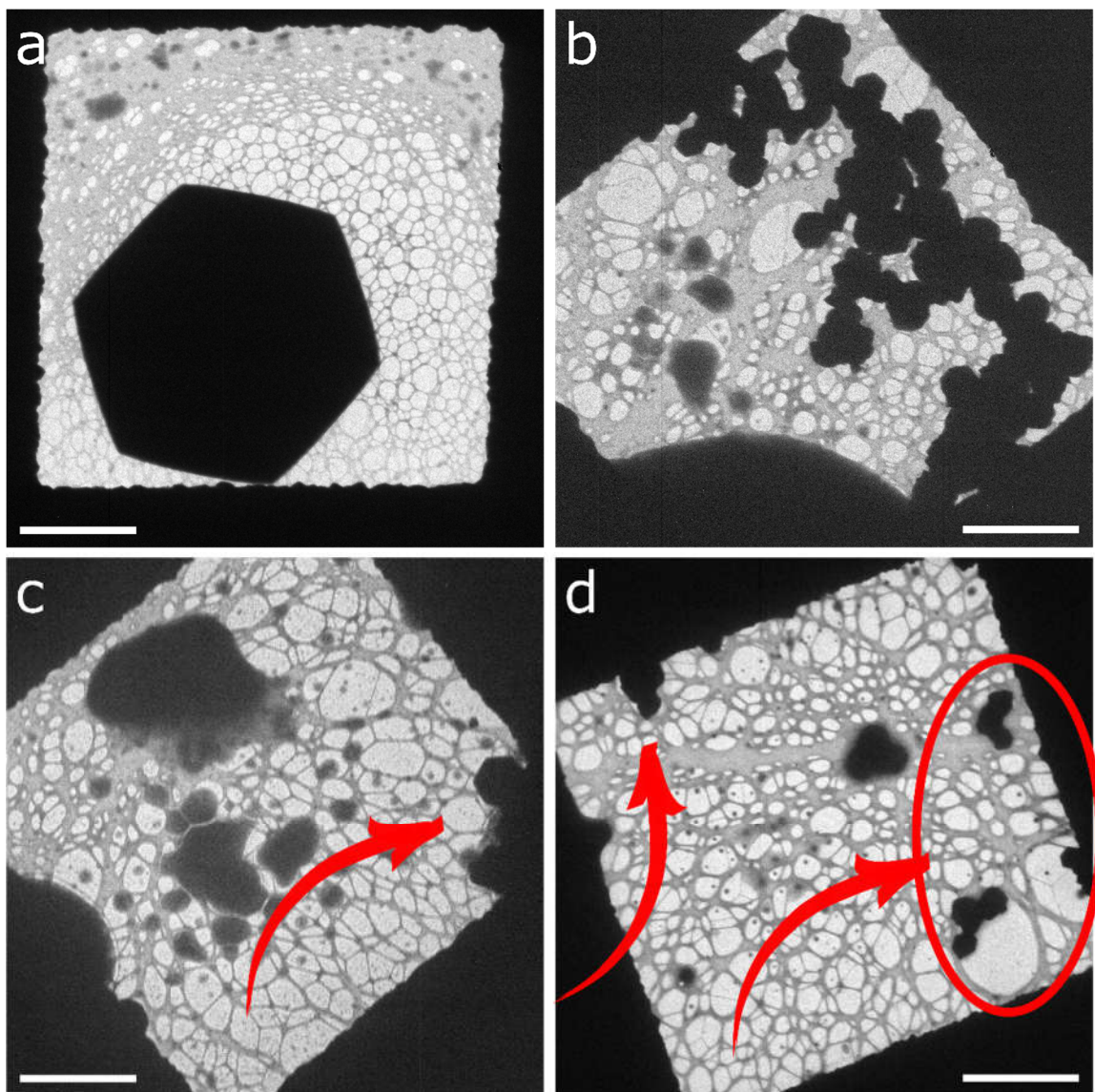
Structures of (a) thiol-modified 4-cysteamino-dC nucleotide used in position four of *BET66-C4-SH* for maleimide conjugation and (b) amino-modified 5-[N-(aminoethyl)-3-acrylimido]-dU nucleotide used in position eight of *BET66-T8-C2N* for NHS-ester conjugation.

Appendix C – Multi-Dye Crystals via Pre- and Post-Crystallization Labeling



Layer-by-layer assembly combined with pre- and post-crystallization methods facilitate creation of crystals with a wide variety of guest molecule arrangements. (a) *BET66/BET66-F* (49:1) core, *BET66/BET66-C4-Cy5* (49:1) shell; (b) *BET66/BET66-C4-Cy5* (49:1) core, *BET66:BET66-Fluor* (49:1) shell; (c) *BET66:BET66-Fluor* (49:1) core, *BET66:BET66-C4-Cy5* (49:1) first shell, *BET66:BET66-Fluor* (49:1) second shell; (d) native *BET66* core, *BET66:BET66-Fluor* (49:1) first shell, *BET66:BET66-C4-Cy5* (49:1) second shell; (e) *BET66:BET66-C4-Cy5* (49:1) core, native *BET66* first shell, *BET66:BET66-Fluor* (49:1) second shell. All images are single slices from confocal z-stacks. Scale bars 100  $\mu\text{m}$ .

*Appendix D – TEM Images of BET66 Crystals Grown On-Grid*



TEM images of *BET66* crystals grown using various combinations of DNA concentrations and buffer conditions. In all cases, a 1:1 mixture of the given buffer and DNA solutions was used when plating the crystal drops, and all buffer variants contained 50 mM lithium chloride. **(a)** DNA: 200  $\mu\text{m}$ , buffer: 120 mM magnesium, 10% MPD. **(b)** DNA: 200  $\mu\text{m}$ , buffer: 480 mM magnesium, 20% MPD. **(c)** DNA: 200  $\mu\text{m}$ , buffer: 600 mM magnesium, 10% MPD. **(d)** DNA: 400  $\mu\text{m}$ , buffer: 240 mM magnesium, 20% MPD. Scale bars 10  $\mu\text{m}$ .

## *Appendix E – FIJI (ImageJ) Scripts for Collecting Shell Growth Kinetics Data*

```
//Begin by making an array that contains all possible boxes, in chunks of 4
lines = newArray(236, 214, 18, 12,
                225, 233, 15, 14,
                251, 233, 18, 14,
                251, 255, 20, 15,
                210, 147, 20, 21,
                241, 143, 21, 19,
                237, 171, 15, 20,
                290, 160, 18, 15,
                306, 183, 22, 15,
                286, 183, 15, 20,
                332, 231, 18, 18,
                323, 257, 18, 18,
                309, 239, 12, 24,
                242, 311, 16, 20,
                272, 305, 28, 18,
                254, 283, 22, 16,
                176, 267, 16, 21,
                198, 288, 19, 22,
                212, 267, 25, 16,
                173, 179, 19, 18,
                160, 208, 19, 23,
                188, 200, 17, 22);

//get slice and frame info so we know how many we are going through
getDimensions(dummy, dummy, dummy, slices, nFrames);

//begin by looping through timepoints of each slice

for (f=1; f<=nFrames; f++) {
//  selectWindow("RT coreshell.tif - RT Coreshell001 - C=0");
//  run("Make Substack...", "current slices=1-64 frames="+f);
  a = getTitle();
  //print("Starting time point "+f);
  Stack.setFrame(f);
  stack_measure = newArray();
  //loop through lines
  //hacked: could use l+=4 instead of l++?
  for (l=0; l<=21; l++) {
    q=l*4;
    makeRectangle(lines[q],lines[q+1],lines[q+2],lines[q+3]);
    measures = measure(a);
    if(measures > 0) {
      stack_measure = Array.concat(measures, stack_measure);
    }
  }
}
```

```

//Now we have all length data for each profile
//Get the mean value out and save to file
//Array.print(stack_measure);
Array.getStatistics(stack_measure, smin, smax, smean, std);

print(f+", "+smean+", "+std);
//print("StdDev: "+std);
//File.append(mean, "results_"+s+"_"+f+".txt");
}

function measure(a) {
  selectImage(a);
  vals = newArray();
  run("Plot Z-axis Profile", "profile=z-axis");
  Plot.getValues(x, y);
  //wait(10);
  //close the annoying plot window
  run("Close");
  Array.getStatistics(y, ymin, ymax);
  for (j=0; j<x.length; j++) {
    //put conditions here
    if ((y[j] >= ymax*0.15) && (y[j] > 2)) {
      vals = Array.concat(x[j],vals);
    }
  }
  Array.getStatistics(vals, min, max, mean);
  diff = max-min;
  if (diff < 0) {
    diff = 0;
  }
  wait(10);
  return diff;
}

```

Script written in FIJI (ImageJ) for recording automatic measurements of base thickness for time-resolved crystal growth monitoring. The thickness of the fluorescent shell is determined by analyzing the z-axis intensity profile through the base and detecting the region above the set fluorescence threshold. Multiple measurements of this type are recorded for each crystal, at different locations around the base.

```

//Begin by making an array that contains all possible lines, in chunks of 4
lines = newArray(273, 233, 424, 86,
                 265, 225, 418, 67,
                 254, 214, 399, 68,
                 269, 256, 467, 306,
                 275, 245, 466, 294,
                 281, 230, 476, 274,
                 226, 236, 71, 357,
                 237, 246, 85, 367,
                 251, 260, 91, 382,
                 236, 207, 16, 151,
                 235, 222, 29, 166,
                 229, 241, 34, 185);

a = getTitle();
//get slice and frame info so we know how many we are going through
getDimensions(dummy, dummy, dummy, slices, nFrames);

//begin by looping through timepoints of each slice

for (s=1; s<=slices; s++) {
  Stack.setSlice(s);
  print("Starting slice "+s);
  for (f=1; f<=nFrames; f++) {
    Stack.setFrame(f);
    //print("Starting time point "+f);
    stack_measure = newArray();
    //loop through lines
    //hacked: could use l+=4 instead of l++?
    for (l=0; l<=11; l++) {
      q=l*4;
      makeLine(lines[q],lines[q+1],lines[q+2],lines[q+3]);
      measures = measure(a);
      if(measures > 0) {
        stack_measure = Array.concat(measures, stack_measure);
      }
    }
    //Now we have all length data for each line
    //Get the mean value out and save to file
    //Array.print(stack_measure);
    Array.getStatistics(stack_measure, smin, smax, smean, std);

    print(f+", "+smean+", "+std);
    //print("StdDev: "+std);
    //File.append(mean, "results_"+s+"_"+f+".txt");
  }
}

```

```

function measure(a) {
  selectImage(a);
  vals = newArray();
  run("Plot Profile");
  Plot.getValues(x, y);
  //wait(10);
  //close the annoying plot window
  run("Close");
  Array.getStatistics(y, ymin, ymax);
  for (j=0; j<x.length; j++) {
//put conditions here
    if ((y[j] >= ymax*0.15) && (y[j] > 9)) {
      vals = Array.concat(x[j],vals);
    }

  }
  Array.getStatistics(vals, min, max, mean);
  diff = max-min;
  if (diff < 0) {
    diff = 0;
  }
  wait(10);
  return diff;
}

```

Script written in FIJI (ImageJ) for recording automatic measurements of side thickness for time-resolved crystal growth monitoring. The thickness of the fluorescent shell is determined by analyzing the intensity profile through the shell and detecting the region above the set fluorescence threshold. Multiple measurements of this type are recorded for each crystal, at different locations on each of the six sides, and at each plane along the z-axis.

## References

1. Jones, M. R., Seeman, N. C. & Mirkin, C. A. Programmable materials and the nature of the DNA bond. *Science* **347**, 1260901 (2015).
2. Winfree, E., Liu, F., Wenzler, L. A. & Seeman, N. C. Design and self-assembly of two-dimensional DNA crystals. *Nature* **394**, 539–544 (1998).
3. Shih, W. M., Quispe, J. D. & Joyce, G. F. A 1.7-kilobase single-stranded DNA that folds into a nanoscale octahedron. *Nature* **427**, 618–621 (2004).
4. Rothmund, P. W. K. Folding DNA to create nanoscale shapes and patterns. *Nature* **440**, 297–302 (2006).
5. Douglas, S. M. *et al.* Self-assembly of DNA into nanoscale three-dimensional shapes. *Nature* **459**, 414–418 (2009).
6. Dietz, H., Douglas, S. M. & Shih, W. M. Folding DNA into Twisted and Curved Nanoscale Shapes. *Science* **325**, 725–730 (2009).
7. Zheng, J. *et al.* From molecular to macroscopic via the rational design of a self-assembled 3D DNA crystal. *Nature* **461**, 74–77 (2009).
8. Ke, Y., Ong, L. L., Shih, W. M. & Yin, P. Three-Dimensional Structures Self-Assembled from DNA Bricks. *Science* **338**, 1177–1183 (2012).
9. Yan, H., Park, S. H., Finkelstein, G., Reif, J. H. & LaBean, T. H. DNA-templated self-assembly of protein arrays and highly conductive nanowires. *Science* **301**, 1882–4 (2003).
10. Park, S. H. *et al.* Three-Helix Bundle DNA Tiles Self-Assemble into 2D Lattice or 1D Templates for Silver Nanowires. *Nano Lett.* **5**, 693–696 (2005).
11. Zheng, J. *et al.* Two-Dimensional Nanoparticle Arrays Show the Organizational Power of Robust DNA Motifs. *Nano Lett.* **6**, 1502–1504 (2006).
12. Sharma, J., Chhabra, R., Liu, Y., Ke, Y. & Yan, H. DNA-Templated Self-Assembly of Two-Dimensional and Periodical Gold Nanoparticle Arrays. *Angew. Chemie* **118**, 744–749 (2006).
13. Aldaye, F. A. & Sleiman, H. F. Sequential Self-Assembly of a DNA Hexagon as a Template for the Organization of Gold Nanoparticles. *Angew. Chemie Int. Ed.* **45**, 2204–2209 (2006).
14. Nykypanchuk, D., Maye, M. M., van der Lelie, D. & Gang, O. DNA-guided crystallization of colloidal nanoparticles. *Nature* **451**, 549–552 (2008).
15. Park, S. Y. *et al.* DNA-programmable nanoparticle crystallization. *Nature* **451**, 553–556 (2008).
16. Gu, H., Chao, J., Xiao, S.-J. & Seeman, N. C. A proximity-based programmable DNA nanoscale assembly line. *Nature* **465**, 202–205 (2010).
17. Serpell, C. J., Edwardson, T. G. W., Chidchob, P., Carneiro, K. M. M. & Sleiman, H. F. Precision Polymers and 3D DNA Nanostructures: Emergent Assemblies from New Parameter Space. *J. Am. Chem. Soc.* **136**, 15767–15774 (2014).

18. Rogers, W. B. & Manoharan, V. N. Programming colloidal phase transitions with DNA strand displacement. *Science* **347**, 639–642 (2015).
19. Li, H., Park, S. H., Reif, J. H., LaBean, T. H. & Yan, H. DNA-Templated Self-Assembly of Protein and Nanoparticle Linear Arrays. *J. Am. Chem. Soc.* **126**, 418–419 (2004).
20. Liu, Y., Lin, C., Li, H. & Yan, H. Aptamer-Directed Self-Assembly of Protein Arrays on a DNA Nanostructure. *Angew. Chemie Int. Ed.* **44**, 4333–4338 (2005).
21. Erben, C. M., Goodman, R. P. & Turberfield, A. J. Single-Molecule Protein Encapsulation in a Rigid DNA Cage. *Angew. Chemie Int. Ed.* **45**, 7414–7417 (2006).
22. Chhabra, R. *et al.* Spatially Addressable Multiprotein Nanoarrays Templated by Aptamer-Tagged DNA Nanoarchitectures. *J. Am. Chem. Soc.* **129**, 10304–10305 (2007).
23. Senesi, A. J. *et al.* Stepwise Evolution of DNA-Programmable Nanoparticle Superlattices. *Angew. Chemie* **125**, 6756–6760 (2013).
24. Lang, J. & Liu, M. Layer-by-Layer Assembly of DNA Films and Their Interactions with Dyes. *J. Phys. Chem. B* **103**, 11393–11397 (1999).
25. Johnston, A. P. R., Read, E. S. & Caruso, F. DNA Multilayer Films on Planar and Colloidal Supports: Sequential Assembly of Like-Charged Polyelectrolytes. *Nano Lett.* **5**, 953–956 (2005).
26. Johnston, A. P. R., Mitomo, H., Read, E. S. & Caruso, F. Compositional and Structural Engineering of DNA Multilayer Films. *Langmuir* **22**, 3251–3258 (2006).
27. Loew, M. *et al.* Controlled Assembly of Vesicle-Based Nanocontainers on Layer-by-Layer Particles via DNA Hybridization. *Small* **5**, 320–323 (2009).
28. Lee, L., Johnston, A. P. R. & Caruso, F. Programmed Degradation of DNA Multilayer Films. *Small* **10**, 2902–2909 (2014).
29. Seeman, N. C. Nucleic acid junctions and lattices. *J. Theor. Biol.* **99**, 237–247 (1982).
30. Paukstelis, P. & Seeman, N. 3D DNA Crystals and Nanotechnology. *Crystals* **6**, 97 (2016).
31. Robinson, B. H. & Seeman, N. C. The design of a biochip: a self-assembling molecular-scale memory device. *Protein Eng. Des. Sel.* **1**, 295–300 (1987).
32. Paukstelis, P. J. Three-Dimensional DNA Crystals as Molecular Sieves. *J. Am. Chem. Soc.* **128**, 6794–6795 (2006).
33. Geng, C. & Paukstelis, P. J. DNA Crystals as Vehicles for Biocatalysis. *J. Am. Chem. Soc.* **136**, 7817–7820 (2014).

34. Camacho, A. S., Martín-García, I., Contreras-Celedón, C., Chacón-García, L. & Alonso, F. DNA-supported palladium nanoparticles as a reusable catalyst for the copper- and ligand-free Sonogashira reaction. *Catal. Sci. Technol.* **7**, 2262–2273 (2017).
35. García-Fernández, A., Megens, R. P., Villarino, L. & Roelfes, G. DNA-Accelerated Copper Catalysis of Friedel–Crafts Conjugate Addition/Enantioselective Protonation Reactions in Water. *J. Am. Chem. Soc.* **138**, 16308–16314 (2016).
36. Soppimath, K. S., Tan, D. C.-W. & Yang, Y.-Y. pH-Triggered Thermally Responsive Polymer Core-Shell Nanoparticles for Drug Delivery. *Adv. Mater.* **17**, 318–323 (2005).
37. Alayoglu, S., Nilekar, A. U., Mavrikakis, M. & Eichhorn, B. Ru–Pt core–shell nanoparticles for preferential oxidation of carbon monoxide in hydrogen. *Nat. Mater.* **7**, 333–338 (2008).
38. Wang, F. *et al.* Tuning upconversion through energy migration in core–shell nanoparticles. *Nat. Mater.* **10**, 968–973 (2011).
39. Li, T., Sullivan, J. E. & Rosi, N. L. Design and Preparation of a Core–Shell Metal–Organic Framework for Selective CO<sub>2</sub> Capture. *J. Am. Chem. Soc.* **135**, 9984–9987 (2013).
40. Ho, L.-C. *et al.* Unibody core–shell smart polymer as a theranostic nanoparticle for drug delivery and MR imaging. *Biomaterials* **37**, 436–446 (2015).
41. Zhao, H.-X. *et al.* Theranostic metal–organic framework core–shell composites for magnetic resonance imaging and drug delivery. *Chem. Sci.* **7**, 5294–5301 (2016).
42. Peng, X. & Schlamp, M. Epitaxial growth of highly luminescent CdSe/CdS core/shell nanocrystals with photostability and electronic accessibility. *J. ...* **7863**, 7019–7029 (1997).
43. Reiss, P., Protière, M. & Li, L. Core/Shell Semiconductor Nanocrystals. *Small* **5**, 154–168 (2009).
44. McPherson, A. & Shlichta, P. J. Facilitation of the growth of protein crystals by heterogeneous/epitaxial nucleation. *J. Cryst. Growth* **85**, 206–214 (1987).
45. Edward, A. M., Darst, S. A., Hemming, S. A., Li, Y. & Kornberg, R. D. Epitaxial growth of protein crystals on lipid layers. *Nat. Struct. Biol.* **1**, 195–197 (1994).
46. Pechkova, E. & Nicolini, C. Protein nucleation and crystallization by homologous protein thin film template. *J. Cell. Biochem.* **85**, 243–251 (2002).
47. Kubo, T., Hondoh, H. & Nakada, T. Epitaxial Growth of Lysozyme on Fatty Acid Thin Films. *Cryst. Growth Des.* **7**, 416–419 (2007).
48. Khurshid, S., Saridakis, E., Govada, L. & Chayen, N. E. Porous nucleating agents for protein crystallization. *Nat. Protoc.* **9**, 1621–1633 (2014).

49. Paukstelis, P. J., Nowakowski, J., Birktoft, J. J. & Seeman, N. C. Crystal Structure of a Continuous Three-Dimensional DNA Lattice. *Chem. Biol.* **11**, 1119–1126 (2004).
50. Saoji, M., Zhang, D. & Paukstelis, P. J. Probing the role of sequence in the assembly of three-dimensional DNA crystals. *Biopolymers* **103**, 618–626 (2015).
51. McNeil, R. & Paukstelis, P. J. Core-Shell and Layer-by-Layer Assembly of 3D DNA Crystals. *Adv. Mater.* **29**, 1701019 (2017).
52. Stevenson, H. P. *et al.* Transmission electron microscopy for the evaluation and optimization of crystal growth. *Acta Crystallogr. Sect. D Struct. Biol.* **72**, 603–615 (2016).
53. Stevenson, H. P. *et al.* Use of transmission electron microscopy to identify nanocrystals of challenging protein targets. *Proc. Natl. Acad. Sci.* **111**, 8470–8475 (2014).
54. Calero, G., Cohen, A. E., Luft, J. R., Newman, J. & Snell, E. H. Identifying, studying and making good use of macromolecular crystals. *Acta Crystallogr. Sect. F Struct. Biol. Commun.* **70**, 993–1008 (2014).
55. Olafson, K. N., Li, R., Alamani, B. G. & Rimer, J. D. Engineering Crystal Modifiers: Bridging Classical and Nonclassical Crystallization. *Chem. Mater.* **28**, 8453–8465 (2016).
56. Hansen, C. L., Skordalakes, E., Berger, J. M. & Quake, S. R. A robust and scalable microfluidic metering method that allows protein crystal growth by free interface diffusion. *Proc. Natl. Acad. Sci.* **99**, 16531–16536 (2002).
57. Whitesides, G. M. The origins and the future of microfluidics. *Nature* **442**, 368–373 (2006).
58. Leng, J. & Salmon, J.-B. Microfluidic crystallization. *Lab Chip* **9**, 24–34 (2009).
59. Zheng, B., Roach, L. S. & Ismagilov, R. F. Screening of Protein Crystallization Conditions on a Microfluidic Chip Using Nanoliter-Size Droplets. *J. Am. Chem. Soc.* **125**, 11170–11171 (2003).
60. Zheng, B., Tice, J. D., Roach, L. S. & Ismagilov, R. F. A Droplet-Based, Composite PDMS/Glass Capillary Microfluidic System for Evaluating Protein Crystallization Conditions by Microbatch and Vapor-Diffusion Methods with On-Chip X-Ray Diffraction. *Angew. Chemie Int. Ed.* **43**, 2508–2511 (2004).
61. Zhang, D. & Paukstelis, P. J. Designed DNA Crystal Habit Modifiers. *J. Am. Chem. Soc.* **139**, 1782–1785 (2017).
62. Kubista, M., Sjöback, R., Eriksson, S. & Albinsson, B. Experimental correction for the inner-filter effect in fluorescence spectra. *Analyst* **119**, 417–419 (1994).
63. Klein, W. P. *et al.* Utilizing HomoFRET to Extend DNA-Scaffolded Photonic Networks and Increase Light-Harvesting Capability. *Adv. Opt. Mater.* **6**, 1700679 (2018).

64. Woller, J. G., Hannestad, J. K. & Albinsson, B. Self-Assembled Nanoscale DNA–Porphyrin Complex for Artificial Light Harvesting. *J. Am. Chem. Soc.* **135**, 2759–2768 (2013).
65. Spillmann, C. M. *et al.* Extending FRET cascades on linear DNA photonic wires. *Chem. Commun.* **50**, 7246 (2014).
66. Yih, T. C. & Al-Fandi, M. Engineered nanoparticles as precise drug delivery systems. *J. Cell. Biochem.* **97**, 1184–1190 (2006).
67. Tiwari, G. *et al.* Drug delivery systems: An updated review. *Int. J. Pharm. Investig.* **2**, 2 (2012).
68. Zhang, D. & Paukstelis, P. J. Enhancing DNA Crystal Durability through Chemical Crosslinking. *ChemBioChem* 1163–1170 (2016). doi:10.1002/cbic.201500610
69. Stahl, E., Praetorius, F., de Oliveira Mann, C. C., Hopfner, K.-P. & Dietz, H. Impact of Heterogeneity and Lattice Bond Strength on DNA Triangle Crystal Growth. *ACS Nano* **10**, 9156–9164 (2016).
70. Ohayon, Y. P. *et al.* 132 Impact of sticky end length on the diffraction of self-assembled DNA crystals. *J. Biomol. Struct. Dyn.* **31**, 84–85 (2013).
71. Heilemann, M., Kasper, R., Tinnefeld, P. & Sauer, M. Dissecting and Reducing the Heterogeneity of Excited-State Energy Transport in DNA-Based Photonic Wires. *J. Am. Chem. Soc.* **128**, 16864–16875 (2006).
72. Su, W., Bagshaw, C. R. & Burley, G. A. Addressable and unidirectional energy transfer along a DNA three-way junction programmed by pyrrole-imidazole polyamides. *Sci. Rep.* **3**, 1883 (2013).
73. MacMillan, A. M. & Verdine, G. L. Synthesis of functionally tethered oligodeoxynucleotides by the convertible nucleoside approach. *J. Org. Chem.* **55**, 5931–5933 (1990).